Spring 2001

Mitigation of Water Vapor Interference for Infrared Polarization-Modulated Gas Filter Correlation Radiometry

David K. Lockwood
Old Dominion University

MITIGATION OF WATER VAPOR INTERFERENCE FOR INFRARED POLARIZATION-MODULATED GAS FILTER CORRELATION RADIOMETRY

by

David K. Lockwood
B.S. May 2000, Old Dominion University
B.A. December 1989, Virginia Polytechnic Institute and State University

A Thesis Submitted to the Faculty of
Old Dominion University in Partial Fulfillment of the
Requirement for the Degree of

MASTER OF SCIENCE

ELECTRICAL ENGINEERING

OLD DOMINION UNIVERSITY
May 2001

Approved by:

Amin N. Dharamsi (Director)

Ravindra P. Joshi (Member)

Glen W. Sachse (Member)

ABSTRACT

MITIGATION OF WATER VAPOR INTERFERENCE FOR INFRARED POLARIZATION-MODULATED GAS FILTER CORRELATION RADIOMETRY

David K. Lockwood
Old Dominion University, 2001
Director: Dr. Amin N. Dharamsi

Gas filter correlation radiometry (GFCR) is a high-resolution, high-specificity technique for sensing gaseous species. A variation of absorption spectroscopy, GFCR has a long-proven record on orbital platforms for quantitative measurements of atmospheric constituents, as well as common usage in ground-based sensing applications. PMGFCR (Polarization-modulated GFCR) is a recent refinement of the technique with several advantages over the traditional method, including reducing the number of photodetectors required, increased sensitivity, and elimination of moving parts.

To date, no infrared remote sensors have successfully measured nitric oxide (NO) in vehicle exhaust due to spectral overlap by strong water vapor (H_2Ov) absorption bands. The inherent specificity of PMGFCR provides sufficient suppression of H_2Ov interference to measure vehicles with high NO emissions (100's parts per million (ppm)).

This thesis investigates optimization of the PMGFCR to further reduce H_2Ov interference. We use a computer model to demonstrate that with careful optical filter selection, accurate measurements of NO are feasible with the PM-GFCR, and optimize a laboratory bench-top PM-GFCR system to verify the predictions made with the computer model. Typical measurement error due to transient water vapor may be reduced from over 300 ppm equivalent NO to as little as 2 ppm.

ACKNOWLEDGMENTS

I would like to take this opportunity to acknowledge the many people and organizations that have contributed to my work in preparing this document, and to the research that led to it.

Dr. Amin Dharamsi, my academic advisor at Old Dominion University as well as the Graduate Program Director for the Department of Electrical and Computer Engineering, has my thanks for his guidance during this research, and particularly for including me on the NASA University Earth System Science project proposal team in the Fall of 1999. My involvement in helping him develop the proposal for the Halogen Occultation Experiment for the Space Station (HALOESS) sparked my interest in this research. Although the HALOESS team was not selected for funding by the UnESS review board, work begun during my undergraduate Senior Design project formed the foundation for this document.

Glen W. Sachse has been my advisor at the Gas Filter Correlation (GFCR) Laboratory at NASA Langley Research Center. Without his direction and encouragement I would never have proceeded with this project. In addition, Glen had the confidence in me to sponsor my admission to the NASA Graduate Student Researchers Program (GSRP), which has lifted the financial burden of attending graduate school. I hope I have fulfilled his expectations during the past year.

On a day-to-day basis at NASA Langley, Mauro (Mario) Rana, Charles Harward, and Tom Slate have given me invaluable help. Particular thanks goes to Mario for his forbearance with my series of novice errors in the lab, and for his skill in showing me better ways to get the work done. If nothing else, because of him I am no longer the

world's worst solderer. Most especially, Mario is responsible for developing the GFCR modeling program and the data acquisition software that are at the core of both the theoretical and laboratory work I have conducted during the past year.

The teams I worked with during my Senior Design classes at Old Dominion contributed to my understanding of the GFCR technique, and to some of the material included in this document. Thanks go to Aubrey Haudricourt, Jim Fay, Ed Heath, Ted Kuhn, Denise Linthicum, Larry Gupton, and Maria Arriaga. Ellen Carpenter, Mark Frye, Stella Harrison, and Byron Meadows have been my friends and study partners for the past four years, and they let me know that if they could do it, I could too.

The Virginia Spacegrant Consortium and the NASA GSRP program have provided me with significant financial support. VSG eased the strain during my pursuit of a Bachelor's degree, while the GSRP allowed me to consider further work toward my Master's.

Thanks Mom and Dad for encouraging me to continue with my education and for the pride you have always shown in every member of our family.

Finally and most importantly I thank my lovely wife Suzanne, who has fully supported my decision to continue with my education after a nearly ten-year hiatus from school. As a friend once said, knowing you has given me a direction in life. Suzanne, I love you, and I hope I can be as supportive when it's *your* turn to go back to college.

TABLE OF CONTENTS

LIST OF TABLES

LIST OF FIGURES

CHAPTER I

INTRODUCTION

1.1 Research Motivation

The world we live in has an enormous capacity to absorb and recycle waste products, a capacity that has been stretched to its limits by industrialization, expanding population, and lack of foresight. Waste products have traditionally ended up in landfills, washed out to sea, or incinerated. Only later, after years of accumulation, do they come to be known as pollution. While many forms of pollution are easily identified and controlled, others are more difficult to manage. Air pollution is one such form; because the atmosphere is so vast and waste just "blows away," it can be difficult to demonstrate that some forms of air pollution actually pose risks. During the 1960's and '70's extreme cases of air pollution in cities such as Los Angeles and Mexico City and the growing environmental movement brought wider attention and research to bear on the problem.

This research bore out suspicions that airborne pollutants contribute to the risk of various cancers, asthma, emphysema, and other chronic illnesses[1]. It was found that oxides of sulfur and nitrogen (SO_x and NO_x) products of combustion combined with water vapor and condensed to make sulfuric acid and nitric acid; leading to acid rain, which has been shown to damage vegetation, man-made structures, and to trigger fish die-offs[2]. Global warming, most likely due to increased carbon dioxide in the atmosphere from man-made combustion processes[3], has been proven a fact.

Recognition of these problems and others contributed to the enactment of the Clean Air Act of 1970 (amended 1977 and 1990), which mandates the phased reduction

of industrial and vehicular air pollutants. As a result of this law and the succeeding improvements to engine efficiency, catalytic converters, and "cleaner" fuel formulations, a 2000 model year automobile emits just 7% as much carbon monoxide (CO), 15% the nitric oxide (NO), and 14% as much hydrocarbons (HC) as a typical car made in 1982[4]. Despite these great improvements, it has been estimated that vehicular exhaust is responsible for 60% of the CO, 29% of the carbon dioxide (CO_2), and 31% of the NO_x introduced into the nation's atmosphere every year[5]. Recent studies by the University of Denver have demonstrated that the worst 10% of vehicular polluters contribute from 50 to 70% of the pollution[6] (depending on gas species); these offenders are called "gross emitters." To attempt to limit pollutants, some states and localities require periodic vehicle exhaust inspections to ensure clean operation. A preferable means of performing these tests would be to use remote sensing; the exhaust plume of a car is analyzed as the vehicle drives past a sensor, eliminating the inconvenience of taking the car to an inspection shop. Such on-site testing also identifies locations that are most prone to vehicular pollution, and can include vehicles whose owners might avoid the requirement for periodic inspections. An effective means of performing such remote sensing is to use infrared absorption spectroscopy, the method used by the University of Denver study, which measured CO_2, CO, HC, and NO. The most common method of making these measurements is to view the infrared absorption in a narrow spectral region in which the target gas is the predominant absorber, and infer the target concentration from the amount of light absorbed. Commercial instruments readily allow such measurements for CO_2, CO, and other species that have strong absorption features in the infrared region. High-resolution remote infrared sensing of NO in a vehicle exhaust plume, however, has been

difficult to achieve because NO infrared absorption bands are overlapped by strong water vapor (H_2Ov) bands. In observing a vehicle exhaust plume, the typical total path effective NO levels are just a few parts per million, while background and transient water vapor may be as high as 4%. Even relatively dry air has a very high mixing ratio of H_2Ov relative to NO. There would be little problem if the overlapping background water vapor level were completely static during the course of a measurement, in which case it would cause no difference signal. However, there are two transient H_2Ov sources while measuring vehicular exhaust. First, the atmosphere is a dynamic system, and breezes carry with them varying amounts of water vapor. Second, and perhaps more importantly, the exhaust plume itself contains about 12% water vapor since the products of stoichiometric hydrocarbon combustion are CO_2 and H_2Ov. Thus the exhaust carries with it a major source of signal interference. In addition, as automotive technology has improved and there is less NO to measure in the plume, a more precise and gas-specific measurement technique is needed than in the past.

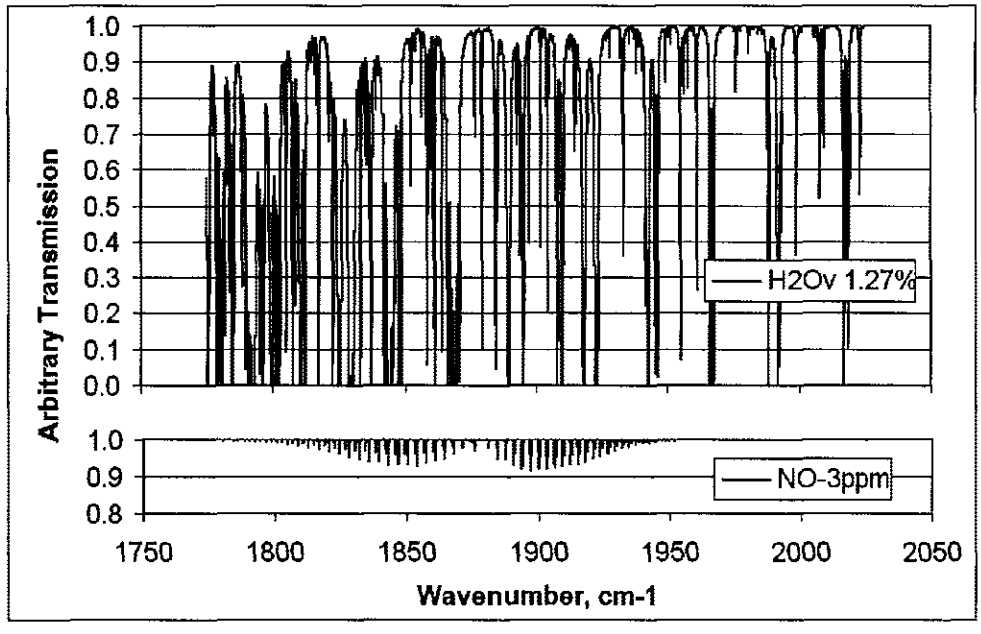

Figure I-1. Infrared Transmission Profiles of H_2O and NO.

The overlapping absorption characteristics of H_2Ov tend to obscure those of NO, as seen in Figure I-1. An important consideration, however, is that although the water vapor and NO possess overlapping spectra in this region, their spectra are not identical since they are different molecules and therefore their line centers and broadening profiles have differences. In such a region of overlap, some means of discriminating the "target" spectrum from the "interference" spectrum is needed.

A successful means of remotely measuring NO has been with a finely tuned ultraviolet (226.5 nm) spectrometer, which can isolate a single absorption line from surrounded features[7]. In order to make simultaneous measurements of the primary exhaust pollutants (CO_2, CO, NO, and HC), both infrared and ultraviolet systems are needed. This is the system currently used in the field. However, since the NO/CO_2 ratio is the desired measurement, simultaneous measurement of both parameters is important. Care must be taken to ensure that the UV and IR sampling beams used have nearly identical interaction with the exhaust plume. If some means can be developed to suppress the H_2Ov interference, it would be preferable to use a single instrument to make all the measurements (CO_2, CO, NO, and HC), simultaneously in the infrared.

Gas Filter Correlation Radiometry (GFCR) is an infrared sensing method under development at NASA Langley Research Center (LaRC) that has promise to allow simultaneous measurement of the primary exhaust pollutants with a single infrared light source. GFCR is inherently target specific, because rather than using just an optical bandpass filter to select the spectral region in which to measure absorption, it uses a sample of the gas itself to act as a "comb" filter. Only the absorption due to the target is seen by the GFCR; most interferences null themselves out by the nature of the

measurements. GFCR has been used to accurately measure a wide variety of atmospheric species from ground and orbital platforms[8], but it has not successfully been used for on-road vehicular exhaust sensing, primarily because this application requires a sampling rate of on the order of 100 Hz. The mechanically switched GFCR does not permit such high rates (i.e., alternatively looking through vacuum and correlation cells). However, recent improvements have been made to the GFCR method, using non-mechanical polarization modulation rather than the traditional method with a mechanical chopper. This highly non-mechanical approach provides path switching at ~50 kHz with a solid-state modulator, allowing increased averaging rates. Combined with highly sensitive photodetectors the PMGFCR permits higher signal to noise ratios than were previously available with conventional GFCR instruments[9, 10]. However, although PMGFCR provides a great deal of specificity, it must be further optimized in order to precisely measure nitric oxide exhaust from newer, low-emission vehicles.

1.2 Research Objectives

The NASA Langley Research Center (LaRC) GFCR laboratory and SPX Corporation have a memorandum of agreement (MOA) to jointly develop a method that will allow rapid, high definition on-road remote measurement of vehicle exhaust NO and other gas species, in a robust, portable PMGFCR instrument. The goal of this research is to contribute to the NASA/SPX project by investigating means of minimizing PMGFCR nitric oxide measurement errors due to water vapor interference. Two specific objectives will lead to achieving this goal:

Objective #1

Experimentally verify that it is possible to null out $H_2O(v)$ interference. The proposed water vapor compensation technique makes use of the positive and negative effect of the interference on GFCR signals, and capitalizes on substantial absorption saturation of the water vapor in our spectral region of interest. Central to the technique is careful selection of an optical bandpass filter that will optimize positive and negative signal interferences to cancel each other out.

Objective #2

Verify the computer-modeled spectroscopy calculations. This goal includes both qualitative and quantitative validation of the system behavior, so that the modeled slope of the GFCR response curve while measuring water vapor interference corresponds to the experimental change of signal intensity with the change of vapor concentration. This model validation is necessary to give confidence in further predictions while developing the GFCR system for other species.

1.3 Summary

We begin in Chapter II with a brief review of the interaction of light and matter, and its application to absorption spectroscopy. This leads to the theoretical basis for atmospheric remote sensing and Gas Filter Correlation Radiometry, followed by the advantages of the new Polarization-Modulated GFCR over the traditional type.

Chapter III discusses modeling the behavior of the proposed PMGFCR system using the NASA LaRC GFCR Response Model, and the component testing performed to verify that the modeling parameters accurately reflect component behavior. Next, this instrument model is used to predict the behavior of the system under a range of

environmental conditions, and measurement variations that will result from modifying the system configuration.

Chapter IV describes the laboratory experiments performed to verify the predictions, including analyses of the data gathered during the experiments. This work is directed toward demonstrating the system's insensitivity to water vapor interference, rather than sensitivity to nitric oxide. Due to the toxicity of NO it is impractical to make actual NO measurements within the laboratory. Experimental agreement with the predictions will confirm the theoretical assertions underlying the predictions, and validate continued development of a commercial instrument utilizing these methods.

The final chapter presents the conclusions derived by the comparison of the experimental results with the theorized and modeled behavior. Work accomplished is evaluated with respect to the research goals. Finally, future goals are presented, including on-road measurements to further validate the interference-compensation technique developed during this research, and a brief description of the continuing work toward constructing a prototype multi-channel commercial polarization modulated gas filter correlation instrument for on-road remote measurement of vehicular exhaust.

CHAPTER II

THEORETICAL DEVELOPMENT

2.1 The Interaction of Light and Matter

Due to the quantum nature of energy, there are discrete energy levels that a molecule can occupy. Energy level transitions are generally expressed as changes to a molecule's rotational (quantum number J), vibrational (quantum number *v*), and electronic states. A jump or drop between energy states E1 and E2 thus has a nominal value of (E2-E1). Photons of the appropriate wavelengths can transfer this energy, and will cause transitions to higher energy levels (absorption, Figure II-1) or will be emitted if the molecule drops to a lower level (spontaneous or stimulated emission). Thus as Einstein described, absorption along with spontaneous and stimulated emission are the three radiative processes by which light interacts with matter.

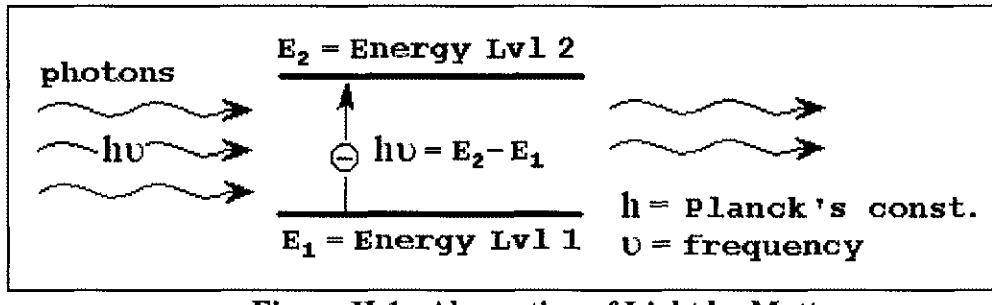

Figure II-1. Absorption of Light by Matter.

Transitions between rotational states generally involve the least energy (>15μm ≈ 0.08eV), vibrational- rotational (VR) transitions typically range from 20 to 2μm (≈ 0.06 to 0.6 eV), while electronic transitions are below 2μm (≈ 1 to 10 eV) [11]. The transition energy is not a strict delta function; it has a finite spectral power density due to line

broadening from several effects. The lineshape function g(ν) describes the broadening mechanisms acting on the transition, and will be described later in more detail.

From the Beer-Lambert law, a beam of light intensity I_o and frequency ν passing through an absorbing medium of length L will be attenuated so that

$$I(\nu) = I_o e^{-\alpha(\nu)L}, \tag{2.1}$$

where the frequency-dependent absorption coefficient $\alpha(\nu) = n\bar{\sigma}g(\nu)$, n is the absorbing species density, $\bar{\sigma}$ is the integrated absorption cross section, and g(ν) is the lineshape function. Assuming weak absorption, equation (2.1) can be approximated [12] by

$$I(\nu) \approx I_o\left[1 - n\bar{\sigma}g(\nu)L\right]. \tag{2.2}$$

The lineshape function g(ν), alluded to earlier, describes the broadening mechanisms acting on a transition. It is important to know the types and degree of lineshape broadening to model and optimize sensor development. There are two major classes of broadening: homogeneous and inhomogeneous. Homogeneous broadening, which equally affects all molecules in a sample, is dominated at atmospheric pressures by collision broadening (also known as pressure broadening). Molecules of types *m* and *n* in a sample are moving randomly with a kT thermal velocity, and have an average collision frequency ν_{col} given by

$$\nu_{col} = N_m \sigma_{col}\left[\frac{8kT}{\pi}\left(\frac{1}{M_m} + \frac{1}{M_n}\right)\right]^{1/2}, \tag{2.3}$$

where N_m is the density of particle type *n* in the sample, σ_{col} is the collision cross section (dependent on the mean free path), and M_m, M_n are the masses of particle types *m* and

n[11]. The Lorentzian lineshape function $g_L(\nu)$ is commonly used to describe homogeneously broadened spectra, and is given by the expression

$$g_L(\nu) = g_h(\nu) = \frac{\Delta\nu}{2\pi\left[(\nu_o - \nu)^2 + \left(\frac{\Delta\nu}{2}\right)\right]}, \tag{2.4}$$

where $\Delta\nu = \frac{1}{2\pi}\left[(A_2 + k_2) + (A_1 + k_1) + 2\nu_{col}\right]$, ν_{col} is the collision frequency per equation 2.3, ν_o is the transition center frequency, and the (A + k) expressions relate to the state decay rates [11]. The ν_{col} part of the $\Delta\nu$ expression dominates, so the collision broadened line width $\Delta\nu \approx \nu_{col}/\pi$.

The primary inhomogeneous broadening source is Doppler broadening, in which the velocity v_z of the particles toward or away from the observer causes a frequency shift. Particles of fundamental frequency ν_o will then be Doppler shifted so that

$$\nu_o' = \nu_o\left(1 + \frac{v_z}{c}\right), \tag{2.5}$$

where c is the speed of light, $3\text{x}10^{10}$ cm/sec [11]. Nearly all conditions are subject to both pressure and Doppler broadening, so it is appropriate to combine the expressions. A group of particles of frequency ν_o and uniform Doppler-shifting velocity v_z will apply a further broadening factor on a homogeneously broadened lineshape $g_h(\nu)$ given by equation 2.5, so that

$$g(v_z, \nu) = \frac{\Delta\nu_h}{2\pi\left[\left(\nu - \nu_o - \frac{\nu_o v_z}{c}\right)^2 + \left(\frac{\Delta\nu_h}{2}\right)^2\right]}. \tag{2.6}$$

However, recalling that the velocities of large quantities of particles in a system are random variables, the Doppler shifted frequencies determined must be assigned to their

respective particles in a statistical manner. The Maxwell-Boltzmann distribution function will give the fraction of atoms with a Doppler-shifting incremental velocity dv_z in the z-direction [11],

$$\frac{dN}{N} = \left(\frac{M}{2\pi kT}\right)^{1/2} \exp\left(-\frac{Mv_z^2}{2kT}\right) dv_z . \tag{2.7}$$

A convolution of equations 2.6 and 2.7, and integrating across all velocities gives the Voigt lineshape function, an expression that combines the homogeneous broadening effect of collisions, with the inhomogeneous Doppler broadening effect [11]:

$$g(\nu) = \left(\frac{M}{2\pi kT}\right)^{1/2} \int_{-\infty}^{\infty} \left\{ \left(\frac{\Delta\nu_h}{2\pi\left[\left(\nu - \nu_o - \nu_o v_z / c\right)^2 + \left(\Delta\nu_h / 2\right)^2\right]} \right) \exp\left(\frac{-Mv_z^2}{2kT}\right) \right\} dv_z . \tag{2.8}$$

Note from expression 2.8, at high pressures the lineshape will be dominated by collision broadening (with $\Delta\nu_h$ maximized by the particle density per equation 2.3). In the low-pressure regime, $\Delta\nu_h$ is minimized, the exponential expression dominates, and Doppler broadening is the primary broadening agent.

Thus to recap, the Voigt Lineshape Function 2.8 can be used as a rather accurate model for the broadening that will occur in air under standard temperature and pressure conditions. Applied to the weak absorption approximation of the Beer-Lambert Law in equation 2.2, one can make predictions about how much signal attenuation a given path length and density of absorbing material will exhibit. Alternatively, knowing the absorption ratio can allow one to make inferences about the nature of the sample. This is the basis of using absorption spectroscopy for remote sensing.

2.2 Remote Sensing

Remote sensing covers a broad range of techniques; all used to measure some parameter from a distance. Small samples can be taken to a laboratory for analysis, but it is frequently preferable to perform measurements on-site. Perhaps the best advantage of using light for remote sensing is that it is the least intrusive means available, minimizing perturbations of the system to be measured, especially for transient phenomena. Measuring the constituents of an air sample is one application where remote sensing is useful. A situation where this is the case is upper atmospheric testing, where it is not feasible to take a direct sample. One means of remotely measuring the particulate components of the atmosphere is by observing the backscatter of a laser beam (LIDAR). Or, an instrument on a satellite can observe the absorption ratio of solar illumination as it passes through the limb of the atmosphere, as the Halogen Occultation Experiment (HALOE) instrument has for over ten years[8], allowing global coverage measuring several gaseous species. Other useful remote sensing applications include probing inaccessible or hazardous locations, such as industrial smokestack emissions monitoring.

As its name implies, absorption spectroscopy is based on photon absorption by a substance. Any given gas species has a unique molecular structure; the interactions between the atoms in the material thus have unique and identifiable energies associated with the transitions between states. For example, the nitric oxide VR transition (v:1→2; J:8.5.→9.5) has an associated wavelength λ of 5.2362μm, or 1909.7835 wavenumbers, where wavenumbers in units cm^{-1} are given by:

$$cm^{-1} = \frac{10,000}{\lambda}, \tag{2.9}$$

and wavelength λ is expressed in units of micrometers ($m * 10^{-6}$). Wavenumbers are convenient units for referring to light, since cm^{-1} units are proportional to energy. If a sample gas is irradiated with and absorbs monochromatic 5.2362μm light, it is most probable that the sample contains nitric oxide. In addition, by knowing the absorption path length and absorption cross-section, the amount of absorption is directly relatable to the amount of NO in the sample, as described earlier.

One method of performing absorption spectroscopy is to use a laser finely tuned to a single spectral absorption feature. This method inherently requires a monochromatic light source, and while it definitely has useful applications, it is not very versatile; to measure several different species one needs either a broad tuning range, or a separate laser system for each target type. One way to make multi-species measurements is to have a broadband light source, and use filters to partition the light to the desired wavelength. Though this method can be used for some molecules, it is subject to errors because it is difficult to manufacture suitable bandpass filters that are economical and efficient. However, there are other means to this end.

2.3 Gas Filter Correlation Radiometry

Gas filter correlation radiometry (GFCR) is a mature technology to allow remote sensing of gaseous species that has been further developed at NASA Langley Research Center. It holds several advantages, foremost of which is its inherent specificity in detecting a target species. Rather than manufacturing a filter to pass only the desired wavelengths as described above, one uses the spectral absorption properties of the target gas to make a "comb" reject filter. A transparent cell is filled with a sufficient pressure of the target gas to be strongly absorbing at each absorption line. Light at all frequencies

other than the target species absorption features will pass through, but the "fingerprint" spectrum of the target molecule is blocked. An identical, but evacuated cell, (or one filled with other gases whose absorption features to not coincide with the sample cell) is placed in an adjacent path. Light is passed alternately through the sample and vacuum cell paths, either by switching the light between them, or by moving the cells.

> Now, if an external {target sample species} cloud is present the signal seen through the gas correlation cell is not affected, since no higher absorption than full absorption can be obtained. On the other hand, the light through the reference channel is reduced due to the absorption lines of the cloud. Thus an imbalance is recorded at the initially balanced lock-in detector[13].

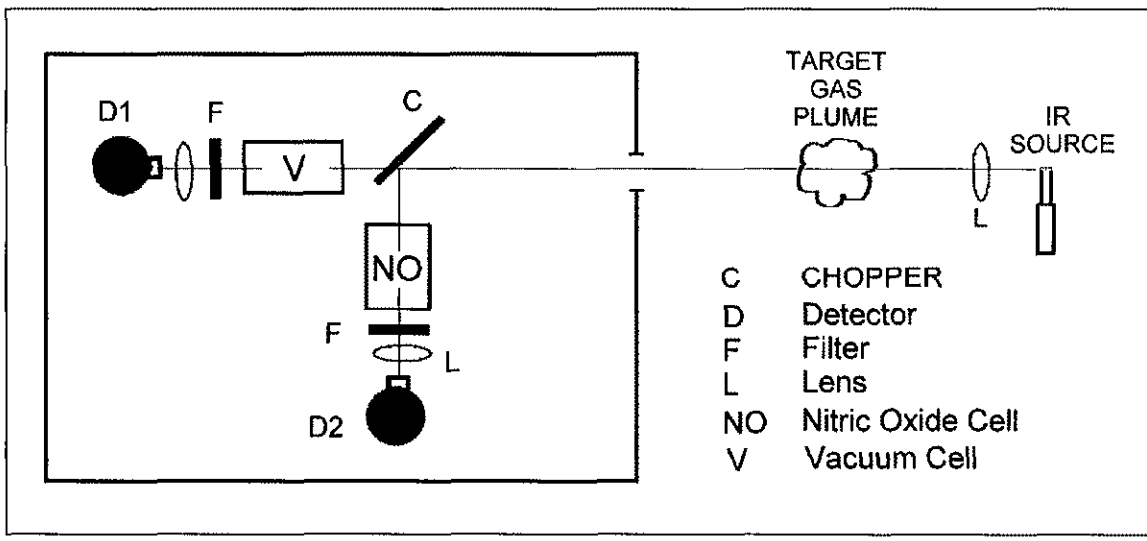

Figure II-2. Single-Channel Mechanically Chopped GFCR Schematic Diagram

Figure II-2 shows a simplified GFCR instrument. The light from the infrared source passes through a path and is attenuated by the target gas plume. The mechanical chopper alternately sends the light through the sample and reference channels. A bandpass filter centered on the region where the signature of the target gas is most pronounced limits the spectral range input to the detector to enhance the measurement

sensitivity to the specific wavelength of interest. The sample and reference paths each have a dedicated photodetector, so particular care must be taken to ensure that the detectors have identical response characteristics so that the differential signal between the two channels is solely the result of the absorption difference between the two paths, and not due to systematic variations.

This method therefore allows a simple analysis to yield the concentrations of the species of interest even in spectral regions where there may be interfering absorption from other atmospheric constituents. It is advantageous that the system be balanced prior to the target plume being introduced into the sample path, since the measurements are based on the path imbalance due to differential absorptions. To this end, a neutral density filter is may be placed in the reference cell path to attenuate it the same percentage as the sample cell. Another common balancing method is to reduce the gain on one of the detectors to achieve signal balancing.

Some "traditional" gas correlation instruments like the one shown in Figure II-2 use mechanical choppers that are reflective on one side to switch between beam paths, but a recent development in gas filter correlation measurements is the use of acousto-optical path switching[10]. In this polarization-modulated gas filter correlation radiometer (PM-GFCR), shown in Figure III-3, after going through the target path, light from the source passes through a polarizer through a photoelastic modulator (PEM, to be described in the following subsection). The PEM rapidly modulates the incoming beam between horizontal and vertical polarization. Next in the path, a polarization-sensitive beamsplitter transmits horizontally polarized light and reflects vertically polarized light, sending each component along separate beam paths. After passing through the sample

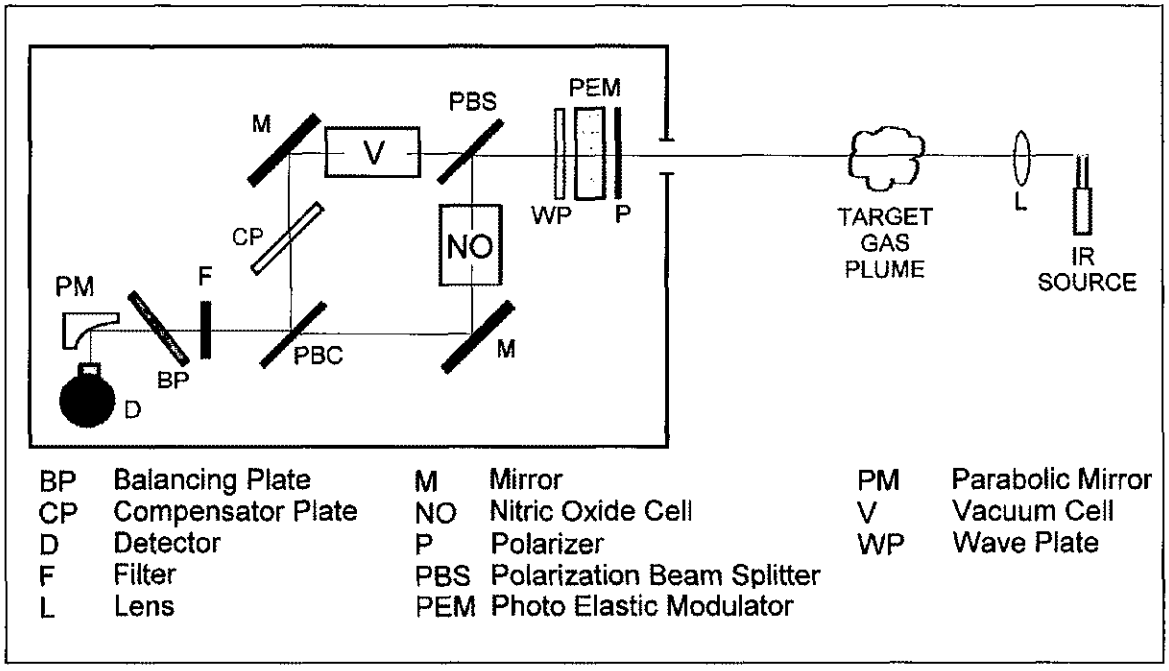

Figure II-3. Single-Channel Polarization-Modulated GFCR Schematic Diagram

and reference cells, the two orthogonally polarized beams are recombined by another beamsplitter before filtering, balancing, detection, and measurement. Similar to the mechanical system, the two channels are balanced to increase sensitivity. This is accomplished by means of a balancing plate, which can be tilted to partially reflect one polarization while transmitting the other. The balanced channels are 180° out of phase, so they combine to a null signal on the detector. However, an imbalance in the channels will cause the sinusoidal signal PEM-modulated signal to be seen at the detector. The intensity of this imbalance signal due to the differential absorption between the paths is proportional to the quantity of the target species intersecting the sample path.

2.4 Photoelastic Modulator (PEM)

The photoelastic modulator alluded to earlier consists of a crystal that is subjected to acoustical compression and expansion via a piezoelectric transducer. This modulation

creates standing compression waves in the crystal, resulting in the creation of time-varying birefringence (i.e., two orthogonal optical axes with refraction indices $n_x(t)$ and $n_y(t)$). By aligning an incident linearly polarized beam to be 45° with respect to the X and Y optical axes, one component of the beam will experience phase retardation with respect to the other component, due to the difference in index of refraction between axes X and Y[15, 16]. The modulation frequency of the birefringence is dependent on the speed of sound through the crystalline material, and on the dimensions of the crystal. The piezo driver modulates the PEM at this resonant frequency, ranging from 30 to 100 kHz, depending on the material and dimensions. The amplitude of the driver power determines the degree of maximum retardation, variously measured in microns, degrees, or wavelengths. The retardation (in length units) is given by

$$A(t)=z\left[n_x(t)-n_y(t)\right] , \qquad (2.10)$$

where z is the thickness of the optical element and $n_x(t)$ and $n_y(t)$ are the instantaneous values of refractive index along the x and y directions[16]. For example, referring to Figure II-4, if the horizontal polarization component of 5.25μm transmitted light is retarded so that it emerges 180° out of phase from its unmodulated state, it has received ½ wave = 180° = 2.625μm retardation. Ignoring for the moment the frequency dependence of

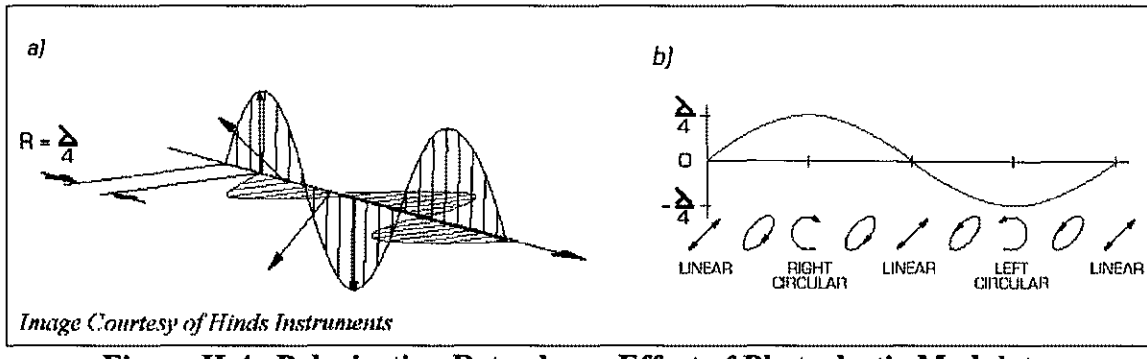

Figure II-4. Polarization Retardance Effect of Photoelastic Modulator

PEM switching efficiency, if light of 10.5μm passes through instead, with the driving transducer set to the same level, the effective retardation will be ¼ wave = 90°=2.625 μm. The retardation effect is continuously modulated from zero to the maximum setting and back, resulting in a quasi-sinusoidal intensity signal for a given output polarization. As illustrated in Figure II-4, at ¼ wave modulation, the transmitted light will cycle through linear, elliptical, and circularly polarized light and back at the 57kHz modulation resonant frequency of this particular PEM.

Optical path switching using the PEM and beamsplitter has been accomplished as fast as 100 kHz (compared to tens to hundreds of Hertz for a typical mechanically chopped GFCR). The PEM used for this research modulates at 57.23kHz. This high switching rate results in several advantages over the more traditional methods including faster response times, and since the measurement is made at a very high frequency, well beyond the spectrum of such noise sources as vibration or turbulence induced noise, greater measurement sensitivity may be achieved[10]. In addition, the solid-state nature of the PEM means it has no moving mechanical parts, resulting in a lighter, more compact, and more reliable system that is not subject to wear over an extended instrument lifetime. This acousto-optical path switching occurs very precisely (e.g., more precisely than a mechanical mechanism that is subject to bearing wobble), therefore not generating additional systematic noise. Also, the polarization-modulated switching method requires only one detector for measuring each species, whereas the "chopped" technique needs two[15]. One drawback is the need to ensure channel balancing to have "zero signal" with the "zero sample" case. As noted earlier, this balancing is also important for the mechanically chopped system, but care must be taken to avoid any undesired polarization

effects in the PM-GFCR instrument. One must be aware of and account for the birefringence effects of all components, particularly since such properties are not always evident.

CHAPTER III

SYSTEM MODELING AND PREDICTIONS

The primary goal of this research is to develop a means of eliminating or compensating for water vapor interference while making PMGFCR measurements of nitric oxide in an automobile exhaust plume. Signal interference may have either a positive or negative effect on the value of the measurements, depending upon how an interfering absorption feature overlaps the absorption spectrum of the gas correlation cell. A preliminary model was thus desired to illustrate how this effect occurs.

It was theorized that there might be spectral regions in which water vapor interference absorption would overlap NO such that there would be equal amounts of positive and negative H_2Ov interference, in effect nullifying itself. In order to determine if such an effect could be achieved, a better model of the interaction between these gas species and how it affects PMGFCR measurements was needed. Such a computer model already existed, having been developed by the NASA GFCR Lab to support their research. Both the preliminary and the full model will be discussed.

3.1 Preliminary Model

Prior to delving into more realistic modeling, a simplified computer model of the GFCR process was made to gain some insight into the process of how interfering absorption lines interact with the correlation cell gas spectrum to generate artifact signal offsets. It was hoped that the model would demonstrate that selection of a proper filter bandwidth and center frequency can take advantage of this positive and negative interference to effectively cancel out the effect of the interfering molecule on the target measurement. Eventually, we plan to show that this method can be used to reduce or

eliminate the obscuring effects of sample path water vapor on gas filter correlation radiometry measurements of NO.

For the simplified model, The HITRAN-PC program (to be described in detail later) was used to model the absorption spectra of NO in a GFCR correlation cell at various partial pressures. In a real NO measurement, there would be about a 300-wavenumber range "in view" of the filter, but to determine the effect of individual lines on a measurement, only a narrow 9-wavenumber region was used. We then created generic simplified interfering absorption lines at two line strengths and entered all this information in an MSExcel file, which applies the GFCR ΔI/I calculations to the simplified absorption spectrum and NO cell data. Having the data in Excel allowed the flexibility to shift the location of the interference data at will. The interfering signal was overlaid on the cell data across a range of frequencies, as illustrated by Figure III-1.

The light intensity $I(\overline{\nu})$ incident on the photodetector at a given wavenumber $\overline{\nu}$, and change in intensity $\Delta I(\overline{\nu})$ due to differential path absorption are calculated from

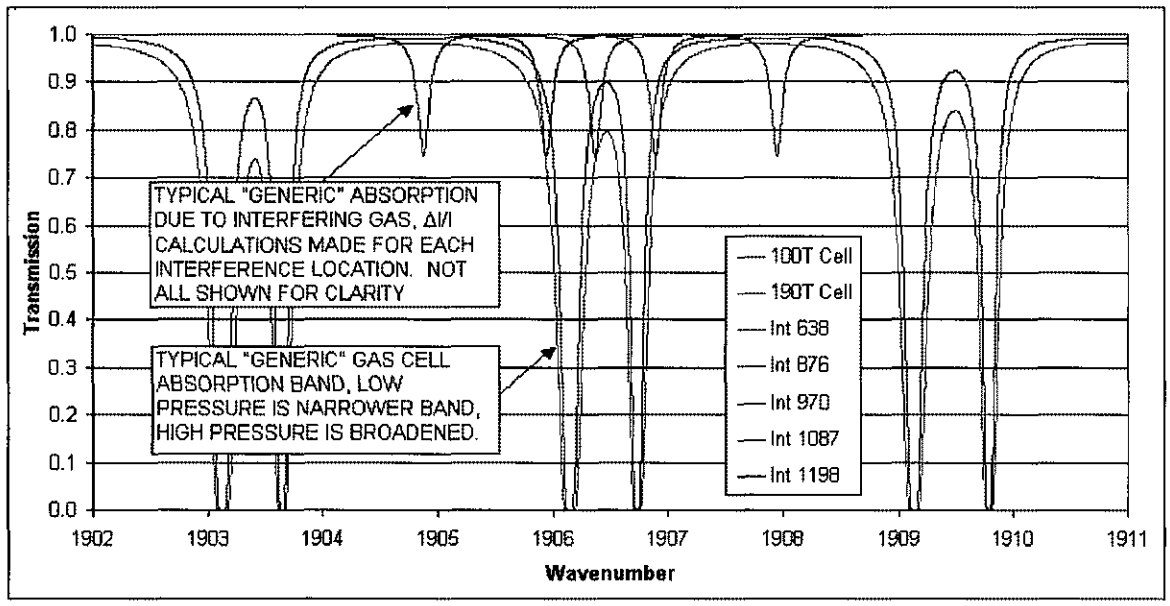

Figure III-1. Simplified Model of Interfering Absorption Lines.

the HITRAN data at the various sample and cell concentrations using the simplified GFCR absorption Equations 3.1 and 3.2 [9], which are simply variants on the Beer-Lambert equation, discussed previously in Chapter II, integrated across the spectral region:

$$\Delta I = I_v - I_c = \int^{spectrum} I_o \cdot \left\{ T_s(\bar{\nu}) \left[T_v(\bar{\nu}) - T_c(\bar{\nu}) \right] \right\} d\bar{\nu}\,, \tag{3.1}$$

$$I = \int^{spectrum} I_o \cdot \left(\frac{T_s(\bar{\nu}) \cdot \left[T_v(\bar{\nu}) + T_c(\bar{\nu}) \right]}{2} \right) d\bar{\nu}\,, \tag{3.2}$$

where $T_s(\bar{\nu})$, $T_v(\bar{\nu})$, and $T_c(\bar{\nu})$ are respectively the transmission of the sample path, vacuum cell, and correlation cell at each wavenumber, calculated from HITRAN data. Note that the signal intensity I_c after passing through the vacuum cell is the initial intensity I_o times the transmission through the sample and through the correlation cell, and similarly for I_v through the vacuum cell. ΔI is simply the difference between these values. The factor of 2 in expression 3.2 is due to the 50% beam splitting; each path is assumed to pass half the initial beam intensity. Since the PMGFCR calculations are based on the ratio of the change in signal (ΔI) to the initial signal (I), I_o is canceled out and thus does not appear in the actual calculation.

$\Delta I(\bar{\nu})$ and $I(\bar{\nu})$ values were calculated for each of the 2000 data points on the 1902 to 1911 wavenumber span used in the model, then averaged arrive at the total spectrum $\Delta I/I$ ratio. The final measure of interest is actually $\Delta\Delta I/I$, the difference between a $\Delta I/I$ measurement when there is no interference (baseline) and the $\Delta I/I$ value with the interference. The Intensity I, change in intensity ΔI, and $\Delta I/I$ ratios were then calculated for each of the eleven positions of the generic the interference absorption line as it was shifted across the correlation cell spectrum. The calculations were then repeated

with a variety of correlation cell NO concentrations from 120 to 200 torr, and with two different interference sample absorptions, with data relations consistent with the low concentration calculations. Figure III-2 shows the result of the ΔΔI/I calculations two values of NO cell pressure (i.e. 120 and 200 torr) for the stronger interferences set.

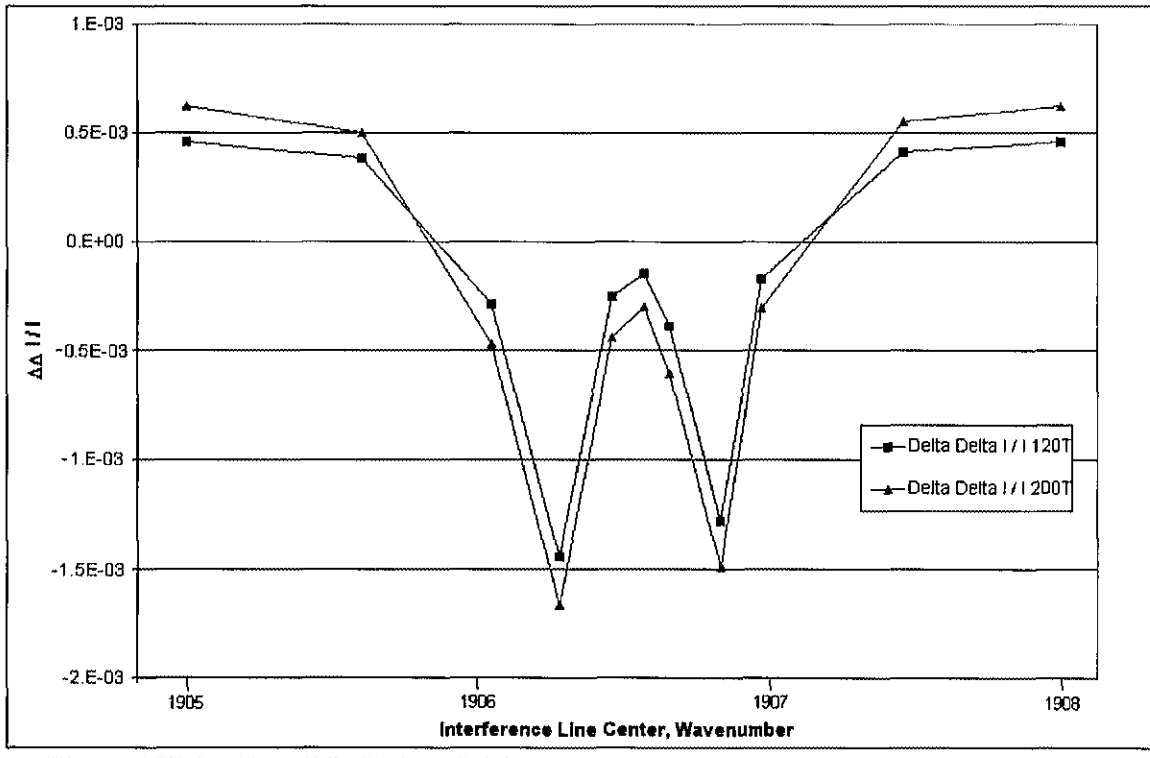

Figure III-2. Simplified Model ΔΔI/I Ratios at Each Interference Line Position

Each color trace is associated with a different correlation cell pressure. This graph shows only the lowest and highest cell pressures; these plots form an envelope around the intermediate pressure cells. It can be seen that the trend is essentially the same regardless of pressure, so once the cell is at saturated absorption, there is little benefit to a higher pressure. Overfill leads to pressure broadening that may overlap undesired spectral features, which would cause a differential signal that cannot be directly compensated. It

is therefore important to know the actual cell pressure, since it does affect the ΔΔI/I signal value, but a broad range of fixed cell pressures will be suitable for use.

At first the vacuum cell was assumed to permit total transmission (i.e., $T_v = 1$). The model was later enhanced to allow a balancing factor to be applied to the system to equalize the vacuum and correlation cell "zero sample" average intensities by applying to the vacuum cell an average attenuation equal to the net correlation cell absorption. In other words, the contents of the correlation cell absorb about 9% of the light passing through, while the empty cell lets the light pass unimpeded. This causes a 9% imbalance between the paths, and will thus look like a large ΔI signal. We wished to verify that applying a balancing factor would normalize the ΔΔI/I signals (change in differential signal measurement) so that the "zero sample" measurement is zero. As will be described later, in practice this effect is accomplished by selectively attenuating the intensity of the vacuum path polarized component, to ensure that the signal difference perceived by the photodetector is due only to the presence of the target gas in the measurement path, not to different cell absorptions.

The ΔΔI/I plots in Figure III-2 cross through zero and have positive and negative values, depending upon where the interfering lines overlap the cell absorption features. In contrast to the quasi-periodic 5.2-micron NO band (doublet lines with relatively wide spacing between each doublet), the H_2Ov band that overlaps the NO lines has many lines of varying line strength and spacing between line centers. As indicated in Figure III-2 some of these will interact with the NO spectrum to generate positive artifact signals, while others will generate negative artifact signals. By moving the bandpass filter location and/or adjusting its width, the sum total of these H_2Ov-NO interactions may

possibly be driven to a net zero effect[15]. Therefore, two factors may be varied to make the net interference cancel out: optimization of filter parameters and to a lesser extent selection of NO cell pressure. The simplified model provided some insight on the effect of varying the H_2Ov lines with respect to the NO lines, and varying NO cell pressures. To calculate where an optimized H_2Ov-cancelling spectral region might really occur requires a more complex model of the PMGFCR operation based on real interference gases and accurate system characteristics.

3.2 LaRC GFCR Response Model

The GFCR Laboratory at NASA Langley Research Center has developed the GFCR Response Model computer program to predict the system behavior. The absorption characteristics of the sample path are modeled by data from the HITRAN database, a continuously updated database of the characteristics of 35 molecular species in the atmosphere. Each molecule has had its rotational, vibrational, and electronic transitions either experimentally determined or calculated. HITRAN is collated from the work of researchers around the world, and its data is generally accepted as valid for modeling the behavior of the gases described. Data for each transition includes the line center wavenumber, molecular isotopes, transition quantum numbers, absorption cross-section, and pressure and self-broadening values[17]. From this information it is possible to calculate the light attenuation along a path of a given length due to a given amount of the absorbing molecular species.

In order to manipulate the data and perform these computation-intensive calculations, we make use of the HITRAN-PC program, developed by the University of Florida and available from the Ontar Corporation. HITRAN-PC has a Windows interface

that allows one to enter path characteristics including multiple absorbing species, the partial pressures of each, total pressure, temperature, path length, wavenumber/frequency range, and the frequency partitioning scale (i.e., how many equally spaced data points to calculate at across the desired frequency range). Depending on the temperature and pressures of the system to be studied, one can select different lineshape functions to make these calculations. As detailed in the previous chapter, we make use of the Voigt lineshape to increase the accuracy of the calculations. HITRAN-PC then calculates the transmission at each wavelength, graphs the data, and makes it available for export to other programs for further manipulation. Typical data output showing the 5.2μm region transmission profiles for H_2O vapor and NO appears in Figure I.1 on page 3. HITRAN-PC has the capability to perform many other types of calculations (atmospheric vertical profiles for LIDAR measurements, high-temperature and pressure emissions, flame spectroscopy), but we have primarily made use of just the transmission plots for our work. Though it is very useful tool, HITRAN-PC is not perfect. The program did not properly incorporate the format changes made to the latest 1996 HITRAN data for nitric oxide,[18] so we had to use the 1992 NO database during the first several months of this work, pending the software patch.

The GFCR Response Model program acts as an overlay on HITRAN-PC. Rather than running separate HITRAN calculations for the transmission profiles of the target gas, interference molecules, and correlation cell contents, all the elements of the path can be entered at one time. In addition, there is an updateable database of filter absorption profiles, detector response functions, attenuations due to optical elements, and photoelastic modulator switching efficiencies. The signal intensity I at each frequency

partition is calculated as a cascade of attenuations due to each system element. The total ΔI/I response per Equations 3.3 and 3.4 (below) is similar to that calculated by Equations 3.1 and 3.2 earlier, and requires numerically integrating across the bandpass of the optical filter used.

$$\Delta I = I_o \int^{filter\_bandpass} T_f(\bar{v}) \cdot T_i(\bar{v}) \cdot T_s(\bar{v}) \left[T_v(\bar{v}) - T_c(\bar{v}) \right] S(\bar{v}) \cdot d\bar{v}, \quad (3.3)$$

$$I = I_o \int^{filter\_bandpass} T_f(\bar{v}) \cdot T_i(\bar{v}) \cdot T_s(\bar{v}) \left\{ \left[T_v(\bar{v}) \cdot D_v \right] + \left[T_c(\bar{v}) \cdot D_c \right] \right\} \cdot d\bar{v}, \quad (3.4)$$

where as before T_s is the wavenumber-dependent transmission through the sample gas, T_v through the vacuum cell, T_c through the correlation cell, and T_i through the interference gas. T_f is the transmission through the optical filter; S is the photoelastic modulator (PEM) switching efficiency; D_v is the intensity signal component for the vacuum cell path; D_c is the correlation cell path intensity signal component; and $d\bar{v}$ is the incremental wavenumber. In Equation 3.2 earlier, both D_v and D_c were assumed to be equal to 0.5, which is an idealized case. Typical calculations integrate over a range of several hundred wavenumbers (wider than the pass band of the optical filter), with 0.005 wavenumber increments. By subtracting ΔI/I for the path with the target gas from the clear path ΔI/I, the ΔΔI/I response is determined. The slope of this response predicts the PMGFCR signal change per target concentration. For the small absorptions caused by NO in the sampling path this response is nearly linear, although at high optical depths the response does go non-linear.

3.3 Component Characterization

In order for the GFCR Response Model to accurately predict the behavior of the system, all of the elements in the optical path must be accurately characterized.

Significant work thus went into verifying exactly how each element of the optical system affects the light passing through it. Once the behavior of the components is determined, numerical models can be generated and incorporated into the program database. The primary elements modeled include the gas cells, filters, balancing plate, and the photodetector. Light transmission through the PEM is wavelength dependent, and determines the "S" parameter in Equation 3.3. The PEM had previously been tested and determined to have optimum switching efficiency in the overall 5.2 μm region with a 99° retardance setting on the controller.

3.3(a) Filters

The primary goal of this research is to determine spectral regions to make GFCR measurements so that water vapor interference is minimized; therefore, optical filter selection is central to the project. The infrared bandpass filters needed for the GFCR measurements are fabricated with multiple layers of dielectric vapor deposition on a suitably transmitting substrate[19], and are very costly with long manufacturing lead times; thus, proper filter selection is also critical for economic reasons and to avoid work delays. During prior work, the transmission profiles of a large number of optical filters had been entered into the database used by the GFCR simulation program. The preliminary calculations performed early in this research made use of ideal square bandpass filters. Once the spectral region with the most promise was determined by these calculations, we were able to decide upon the optimum real filters to use. Based on the preliminary calculations, it was decided that an off-the-shelf filter designed for Nitric Oxide measurements and already available at the lab would be suitable for our proposed experiments. This was preferable to having a filter custom made, since it saved

considerable time and money. The filter used is centered at 5.22 μm, with a 230-wavenumber full width at half max (FWHM). The spectral overlap of the filter over the 5.2-micron NO correlation cell spectrum is shown in Figure III-3.

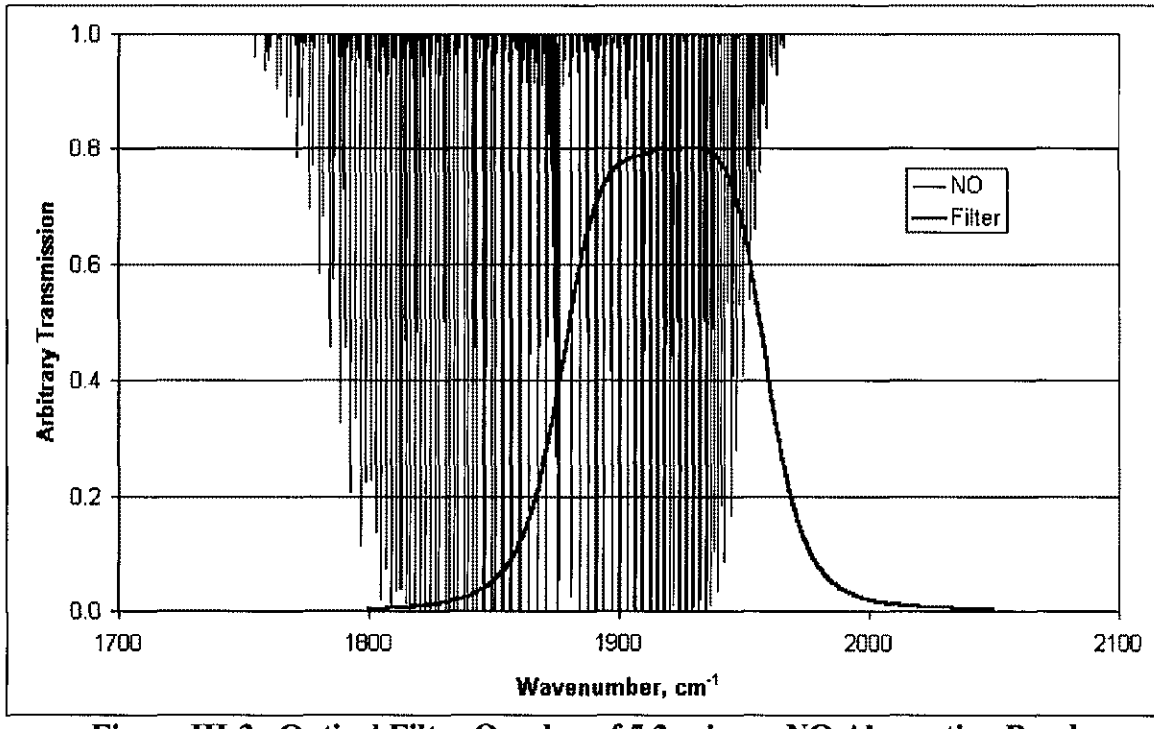

Figure III-3. Optical Filter Overlap of 5.2-micron NO Absorption Band

Luckily, tilt-tuning the filter can modify these characteristics, so there is some degree of flexibility. The transmission of an interference filter is broadened and shifted toward shorter wavelengths if used at an inclined angle. The new transmission center wavelength λ_θ is approximately related to the nominal wavelength λ_o by

$$\lambda_\theta \approx \lambda_o \frac{\sqrt{n^2 - \sin^2\theta}}{n}, \tag{3.5}$$

where θ is the angle of incidence and n is the substrate material index of refraction[13]. Rather than calculating the filter shift range available, it was more direct and accurate to actually measure it.

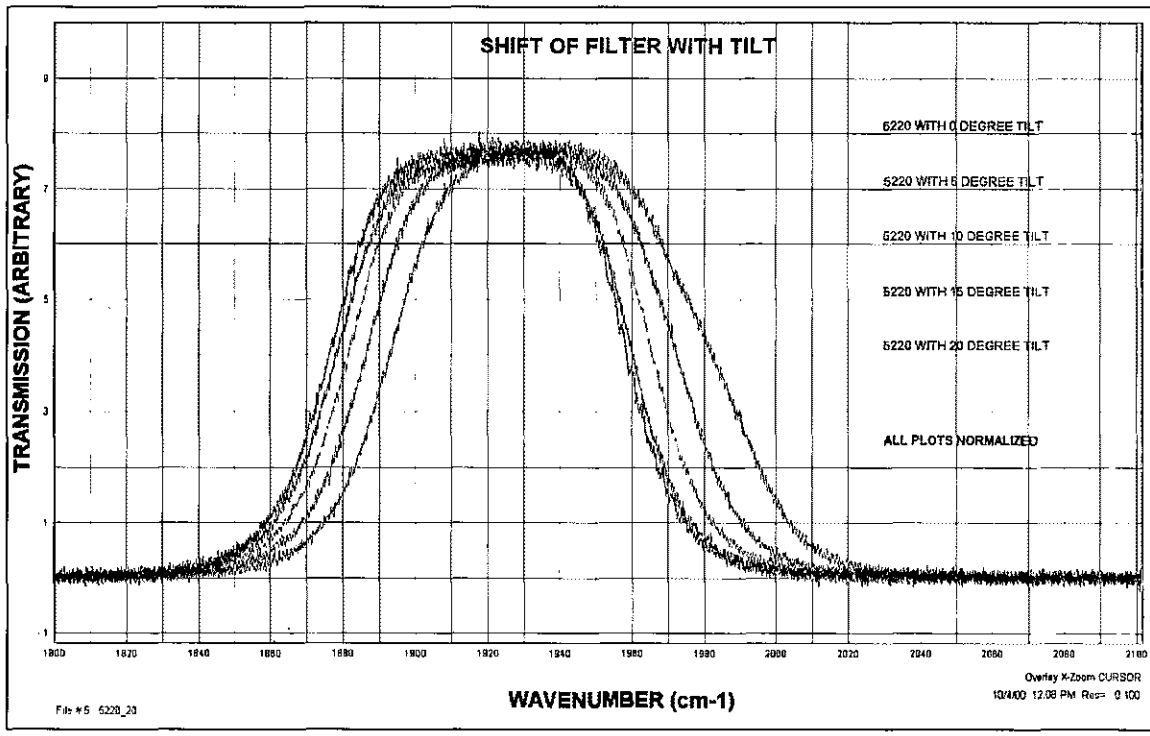

Figure IIII-4. Interference Filter Wavenumber Shift with Tilt.

To make these measurements, we used the Bomem Fourier Transform Infrared (FTIR) spectrometer to scan the filter tilted at 0, 5, 10, 15, and 20 degree angles of incidence of unpolarized light. We were able to confirm that the filter bandpass was per the manufacturer's specifications, and that Equation 3.5 would give somewhat accurate predictions, if based on a 2.3 refraction index. However, the substrate material is sapphire (Al_2O_3) with a 1.77 index of refraction. We were unable to account for this disparity from the formula.

Table III-1. Interference Filter Wavelength Shift with Tilt

Tilt Angle	FWHM, nm	Center λ, nm	Center λ Shift, nm
0	226	5218	Baseline
5	228	5214	4
10	235	5202	16
15	234	5185	32
20	245	5163	55

As shown in Figure III-4 and Table III-1, the filter bandpass region did indeed shift toward shorter wavelengths (higher wavenumbers), but there was also a significant distortion of the absorption curve shape. Manufacturer's data indicated that such distortion would occur at angles of incidence exceeding about 30 degrees, but it is very noticeable in the 20^{o} tilt scan.

Therefore, rather than just shifting the "normal" filter data over in wavenumbers when modeling the tilted filter, we made a separate filter data file for each shifted position, in order to include the distorting effects due to tilt when making the calculations. As will be described later in the Chapter IV experimental section, the care we took to ensure accurate filter tilt modeling was not sufficient to correctly simulate the system behavior, and contributed to the disparity between the simulated and experimental signals.

3.3(b) Gas Cells

The gas cells planned for use with the GFCR prototype are one-inch (2.54cm) long glass cylinders, with 7/8-inch diameter sapphire windows at each end, and a glass tube stem, used to fill the cell. These cells were chosen for several reasons: First, they are readily available, the windows have good transmission through the mid-infrared, and the materials are non-reactive with the gases to be used. Simulations using HITRAN-PC indicated that a 1" length was sufficient for the NO absorption to saturate at achievable pressures and concentrations. Simulations were run with the cell fill at 50 through 300 torr, in 50 torr increments. Once a fill level is reached where saturation occurs, there is little benefit to having a longer cell or higher pressures. In addition, overfilling will cause increased pressure broadening of the absorption profile, which may lead to

overlaps with undesired spectral features. For example, a water vapor transition adjacent to a nitric oxide absorption line will look the same to both channels on the GFCR since it is absorbing in both cells. However, if the sample cell is oversaturated and the NO absorption band spreads over the water line, a difference signal will be read by the detector when water vapor is in the beam path. This signal will effectively be measuring water vapor, and is thus an undesired artifact in the nitric oxide measurement system. The perfect sample cell will thus be filled to just short of saturating, so that sensitivity to NO will be maximized. Unfortunately, there are unavoidable overlaps with water vapor, but as the simplified model demonstrated in the previous section, there are both positive and negative difference signal effects, much of which will cancel each other out. To compensate for the remainder of the imbalance, proper filter selection is vital, as described previously.

The simulations had indicated that the optimal cell fill pressure would be about 200 torr, so several cells were sent to a supplier with the facilities for controlled filling at this level. Unfortunately, delivery was delayed due to supply and equipment problems at the supplier's lab. The delivered set of cells had only one cell suitable for use, since

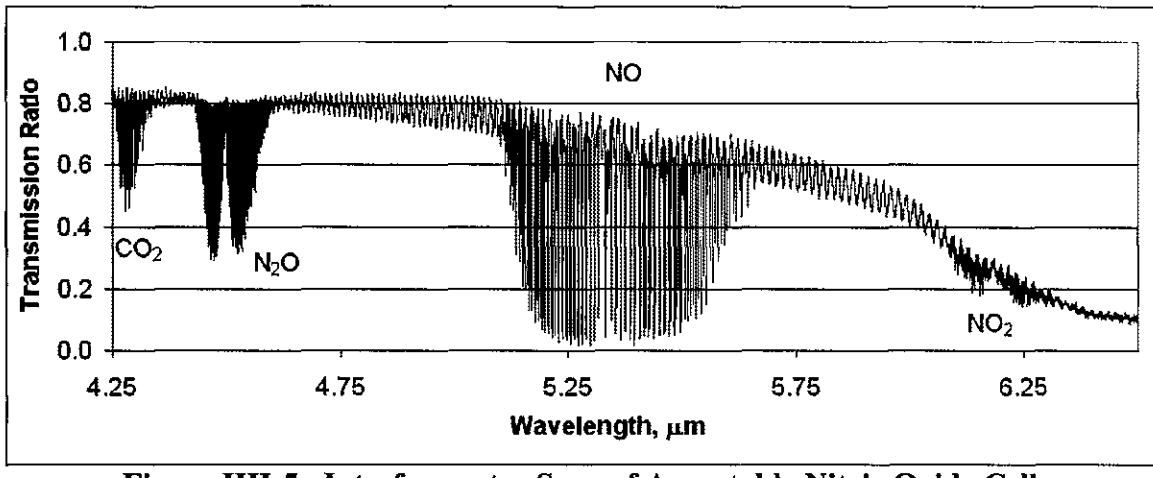

Figure IIII-5. Interferometer Scan of Acceptable Nitric Oxide Cell.

scans we performed with the Bomem FTIR spectrometer revealed unacceptable conditions in the others. As seen in Figure III-5, the correct sample cell has strong absorption in the NO region centered at 5.3 μm. The small amounts of CO_2, N_2O, and NO_2 are expected contaminants as described in the gas supplier's published data[20], and are acceptable for our usage. The properly filled cell was suitable for use in the planned laboratory experiments, but we had wanted to make measurements with several different cells to demonstrate a more flexible system that would readily allow swapping cells if the need arose.

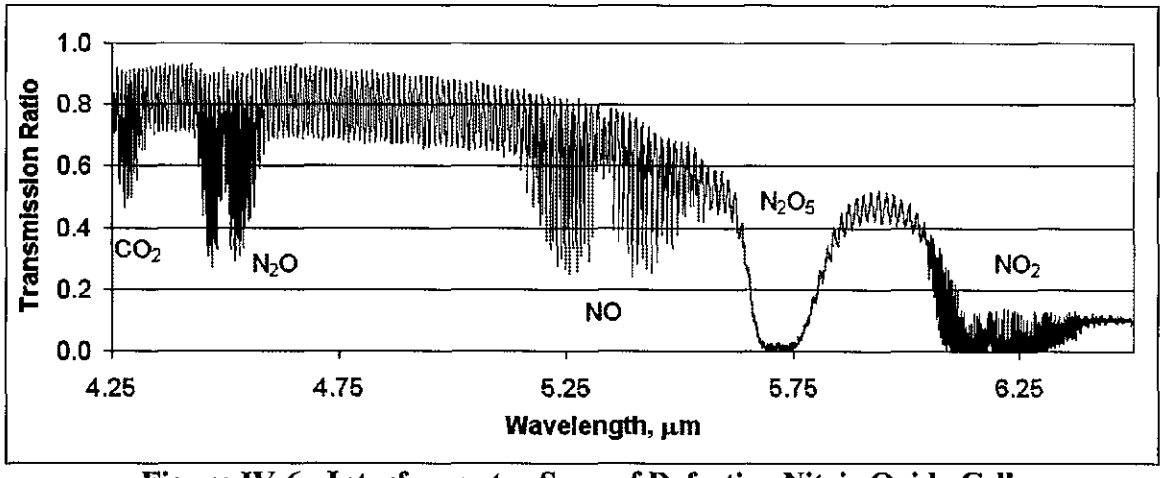

Figure IV-6. Interferometer Scan of Defective Nitric Oxide Cell.

The scan of a rejected cell shown in Figure III-6 demonstrates much weaker absorption by NO, and strong absorption features around 5.75 and 6.25 μm. This particular cell had a few torr of oxygen deliberately included in the mix, which as expected reacted with the NO to make NO_2. The plan was to make a cell that would allow both NO and NO_2 measurements, by splitting the sampling beam with edge filters to direct it to separate detectors for each target gas (the commercial instrument eventually planned will have a filter array to partition the beam for several different target gases).

However, too much oxygen was introduced into the mix, reacting with more NO than desired and leaving too little nitric oxide for confident measurements. In addition to forming NO_2, the oxygen unexpectedly also reacted to form N_2O_5, which is responsible for the 5.75 μm absorption region (identified from the scan by a chemist working nearby[15]). The N_2O_5 absorption feature will presumably appear in future attempts to make the "combination" cell, but it is far enough outside the spectral regions to be targeted for NO and NO_2 that it is not expected to interfere with their measurements. Future attempts to make NO-NO_2 combination cells will decrease the amount of O_2 added in order to create less NO_2 and N_2O_5 in the cell, and leave more NO.

An additional potential problem noted during the FTIR gas cell scans was the high frequency "ringing" (the ripple on the scan lines). This is attributable to etaloning, in which some of the light passing through the cell windows reflects inside and bounces back and forth before continuing through. Putting a slight tilt (wedge) to the windows when they are attached to the cell can mitigate the etaloning. The ringing effect was included in the computer model of the cells and made no noticeable difference in calculation results, and since we had only one properly filled cell, we continued with it.

After the spectral scans to ensure proper cell fill, the filled sample cell and empty vacuum cell were placed in the PMGFCR assembly to check their relative absorptions. The "blocked path" signal due to the surrounding background (stray light and thermal effects picked up by the detector) is gathered by blocking the infrared beam. As shown in Table III-2, the V' values are the measured signals, while the V values are the contribution only from the infrared beam. The V/V_o ratio gives the cell absorption; the difference between the sample and correlation cell values indicates the absorption due

specifically to the NO in the sample cell, since the cells are otherwise identical. As a check, the tests were performed using both the transmitted and reflected beam paths; both routes indicated 9.1% more absorption by the sample cell. This finding was consistent with the 9.3% absorption predicted by modeling with HITRAN-PC. The model calculation was based on the 200 torr design pressure. The measured versus predicted absorption difference may be attributable to uncertainty in the actual partial pressure of NO in the cell, since we relied on pressure level information provided by the contractor who filled the cell.

Table III-2. Gas Cell Transmission Test Data

Transmitted Path			All V values are Volts			
Blocked Path DC Volts V_{bp}	Without Cell $V_{o'}$	Beam Signal $V_o = V_{o'} - V_{bp}$	Correlation Cell $V_{c'}$	Correlation Cell $V_c = V_{c'} - V_{bp}$	NO Sample Cell $V_{s'}$	Sample Cell $V_s = V_{s'} - V_{bp}$
0.484	1.244	0.760	1.025	0.541	0.956	0.472
$V_c / V_o = 0.712$		$V_s / V_o = 0.621$		$(V_c - V_s) / V_o =$	**0.091**	

Reflected Path			All V values are Volts			
Blocked Path DC Volts V_{bp}	Without Cell $V_{o'}$	Beam Signal $V_o = V_{o'} - V_{bp}$	Correlation Cell $V_{c'}$	Correlation Cell $V_c = V_{c'} - V_{bp}$	NO Sample Cell $V_{s'}$	Sample Cell $V_s = V_{s'} - V_{bp}$
0.541	1.256	0.715	1.031	0.490	0.966	0.425
$V_c / V_o = 0.685$		$V_s / V_o = 0.594$		$(V_c - V_s) / V_o =$	**0.091**	

The 9.1% absorption difference between the sample and correlation cells, highlighted in Table III-2, will cause a path imbalance that may be compensated to enhance measurement sensitivity. One easy rough compensation method is to place the correlation cell in the reflected path, and the sample cell in the transmitted path. The beamsplitters are specified to be 50/50, but as seen by comparing the V_o values in Table III-2, actually about 6% more light passes through the transmitted path. Putting the

more-attenuating sample cell in the transmitted side results in a net imbalance of only about 4%, which will be compensated for by the balancing plate.

3.3(c) Balancing Plate

As indicated earlier, a method is desired to ensure that the reflected and transmitted paths are balanced when the sampling path is clear of any target gas. In mechanically chopped GFCR system described earlier, the two paths are easily balanced by placing a neutral-density filter in one path, or by reducing the gain of one of the detectors. However, the prototype under design has multiple channels, each viewing a different wavelength of light from the infrared source. Each of these wavelengths will have a different amount of attenuation upon passing through the gas cells, so each species path needs to be individually balanced, after being split from the other wavelengths. In order to do so, a polarization-sensitive balancing mechanism is needed, since the reflected and transmitted beams (horizontally and vertically polarized beams) are recombined into a single beam by this point in the path and cannot be selectively attenuated with a neutral-density filter. To achieve this function, a balancing plate (i.e., a tilted infrared transmissive window) may be used.

The amount of reflection an electromagnetic wave experiences at a dielectric boundary is dependent on the polarization state of the wave, the angle of incidence, and the refractive indices of the materials. Light with a polarization vector parallel to the plane of incidence (p-orientation) as it propagates from a medium with index n_1 (equal to 1 for air) into another with refraction index n_2 transmits differently from light having its polarization vector perpendicular to the plane of incidence (s-orientation). The difference

in transmission of s- and p-wave polarization components is strongly dependent on angle of incidence. This balancing plate mechanism thus allows selective attenuation of a given polarization passing to the detector by tilting the plate. A 4" diameter Calcium Fluoride (CaF_2) window was available at the lab, and as expected its 1.44 refractive index allowed sufficient polarization selectivity for our needs. Rough balancing was readily achieved by tilting the plate until the sinusoidal difference signal on the oscilloscope display disappeared into the noise background. By mounting the window on a micrometer-adjustable rotating stage, fine balancing of the two polarization paths can be achieved.

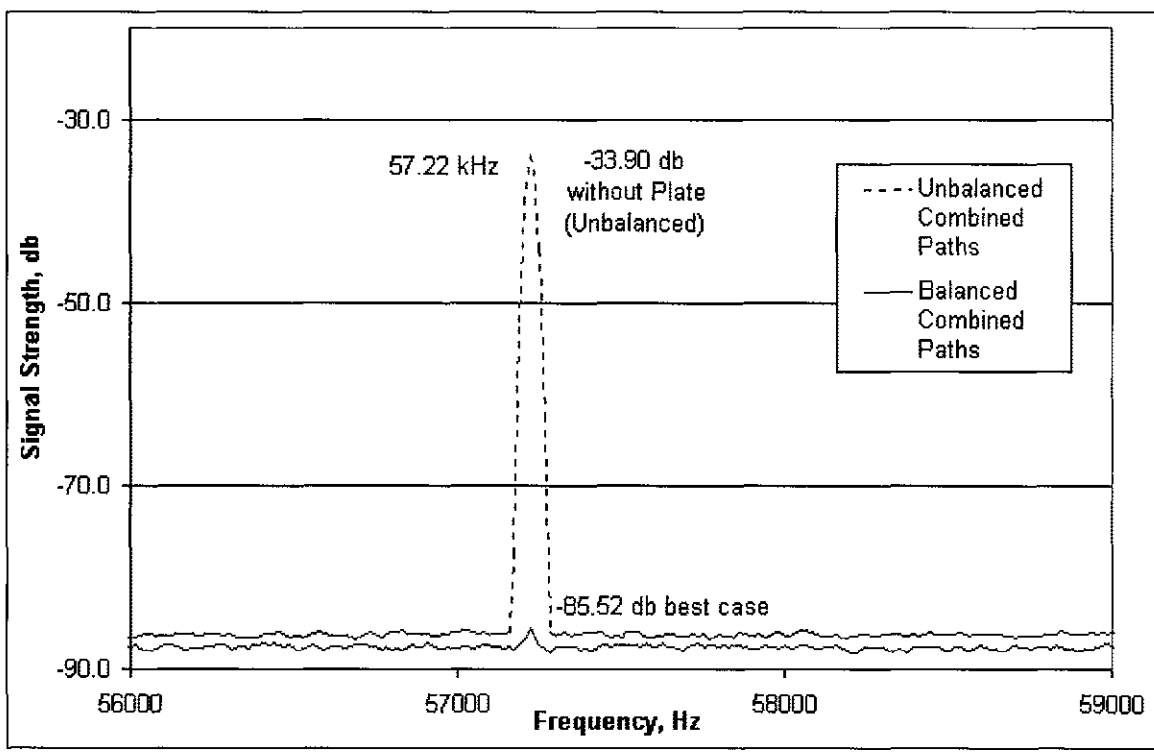

Figure III-7. CaF_2 Balancing Plate Combined Paths Noise Attenuation

To help optimize the balancing, the detector output was connected to a Stanford Research Systems SR760 Fast Fourier Transform Spectrum Analyzer, triggered by the 57.22kHz PEM reference signal. The spectrum analyzer allows better discrimination of

the 57 kHz signal than "eyeballing" the scope; thus, finer balance tuning was achieved. This instrument also has GPIB and serial output ports to allow measurement data to be sent directly to a data acquisition computer. As seen in Figure III-7, the unbalanced 57.22 kHz signal measured approximately -34 db in a -87 db noise environment, which the rough balancing could typically improve to about -70 db. Optimal adjustment of the balancing plate allowed a (85.52-33.90) = 51.62 db best-case improvement in eliminating path imbalance. This corresponds to a $10^{2.49}$ = 380 times improvement. Average maintained balancing is around -82 db, approximately 250 times attenuation improvement versus without the balancing plate.

The system was repeatedly observed to maintain fine balancing for over four hours, as long as background water vapor levels did not vary appreciably. This is also about how long the liquid nitrogen dewar for the photodetector stays full; beyond this time the detector is no longer stable until refilled. Refilling the detector temporarily unbalances the instrument, mainly because the LN_2 chills the optics, causing them to contract and lose alignment. After about 20 minutes the system warms up to the ambient conditions at which it was initially balanced, and comes close to proper balance. Once suitable thermoelectrically cooled detectors are incorporated into the nitric oxide measurements the balancing will be more stable, since there will be no need for periodic coolant filling. Significant changes in background water vapor levels do imbalance the measurement as expected.

3.3(d) Photodetector

The photodetector planned for use with the commercial instrument will be a photovoltaic mode thermoelectrically cooled mercury cadmium telluride type. This

configuration offers the great benefit of continuous operation in a wide range of thermal environments, with little need for user interaction. The thermoelectric cooler is electronically set to maintain a detector temperature of approximately -80° C, which significantly reduces thermal *kT* noise versus operation at room temperatures. This type of detector was ordered for use with the commercial instrument, but for the laboratory experiment we made use of a liquid nitrogen (LN_2) cooled photovoltaic mode Indium Antimonide (InSb) detector, Judson Model J10D. The InSb detector operates at 77 Kelvin (the temperature of LN_2) and offers excellent sensitivity.

3.4 Measurement Predictions

The previous work with the preliminary model validated moving forward with a more realistic model of the GFCR process, using real water vapor interference values on the NO spectrum proposed for the GFCR instrument. The objective of this phase of work is to determine that the positive and negative effects of H_2Ov interference that were simplistically illustrated using just a few gas cell absorption lines and one interference line at a time would have similar effects with a real system with a large number of irregularly spaced lines. If so, a target filter bandpass region could be found such that changes in background water vapor concentration would have minimal effect on the NO measurements, despite the spectral overlap of the H_2Ov and NO absorption bands.

A series of simulations were conducted with the NASA LaRC GFCR Response Model, using parameters based on roadside remote sensing of automobile exhaust. In this scenario, illustrated in Figure III-8, the instrument would be on one side of a highway off ramp; the infrared beam crosses the road and passes through the vehicle exhaust plume to a retro reflector that sends the beam back to the instrument for analysis.

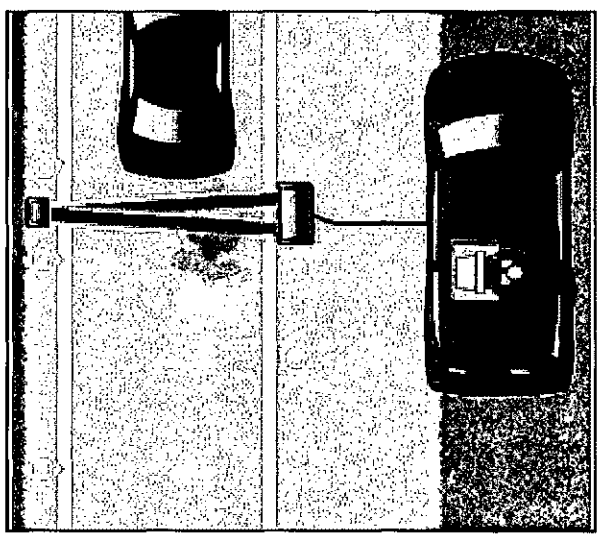

Figure III-8. Roadside Remote Sensing

The total path length is about 50 feet, (15.24 meters), with the exhaust plume width as it exits the tail pipe on the order of 2 inches (5 cm). An important consideration is that the beam is traversing the entire path length, but we wish to attribute any measurements only to perturbations by the 5 cm plume.

To compute the GFCR signal effect due to a water vapor change in the plume, it is first necessary to determine the effective total path percent of water vapor due to water vapor from the exhaust plume. This is because the GFCR modeling program (and the actual instrument) only "sees" total path changes, not where in the path the changes actually occur. This value is calculated per Equation 3.6:

$$C_{eff} = \frac{(L_t \cdot C_b) + \left[L_p (C_p - C_b) \right]}{L_t} \tag{3.6}$$

L_t = Length of total path, meters L_p = Width of tailpipe, meters

C_b = Concentration of background H_2O % C_p = Concentration of plume H_2O %

C_{eff} = Total path averaged H_2O including H_2O in exhaust, %

The percent water vapor in a typical exhaust plume is assumed to be 12%, based on data from the Society of Automotive Engineers (SAE). Percent values of H_2O calculated by Equation 3.6 are converted to parts per million to be compatible with the GFCR modeling program (1% = 10,000 ppm). Table III.3 indicates the path averaged H_2Ov in the total path due to the plume for varying levels of background water vapor, as determined by Equation 3.6.

Table III-3. Effective Water Vapor in Total Path Due to Plume

H_2O% Background	H_2O ppm Background	% + Plume @ 12% Effective in Path	ppmv + Plume @ 12% Effective in Path
0.0	0	0.039370079	393.7
0.05	500	0.089206037	892.1
0.1	1000	0.139041995	1390.4
0.3	3000	0.338385827	3383.9
0.5	5000	0.537729659	5377.3
1.0	10000	1.036089239	10360.9
1.5	15000	1.534448819	15344.5
2.0	20000	2.032808399	20328.1
Note:	15.24 meter path, 5 cm plume, 12% H2Ov in plume		

Early calculations using an ideal bandpass filter model had indicated that a filter available at the laboratory had the potential to meet our needs. This filter, centered at 5.22 μm with a 0.23 μm bandpass, has been described earlier. The numerical model of the filter was used in the calculations, including the distortions caused by tilt tuning.

The simulations were an iterative process; with the ΔI/I calculations run first with the filter set normal to incident light, for a clear path with only the interference H_2Ov (e.g., 20000ppm per Table III-3), then with the addition of an exhaust plume to the path (3 ppm NO "target," and total 20328.1 ppm H_2Ov). Three ppm NO in the total path is equivalent to 914 ppm NO present only in the plume, based on the total path / plume length ratio = 15.24m / 0.05m = 304.8 multiplier. As discussed earlier, the GFCR system signal/target concentration response is determined by the slope of the line between the ΔI/I values with and without the target in the path. It is evident that the system response must be linear to allow straightforward conversion of the detector signal to target gas concentration. As will be shown, the predictions validated the use of this approximation, since only relatively small perturbations occur during most measurements.

Similar calculations are then run with incrementally increasing levels of background water vapor. All simulations shown were performed under standard conditions of 22°C and 760 Torr. Later calculations address changes to these conditions. The entire process is repeated with varying filter positions; in the case of Figure III-9, three-wavenumber increments from 0 to 24. Although Figure III-9 is "busy," it illustrates several concepts affecting the goal of water vapor error compensation, and warrants close examination.

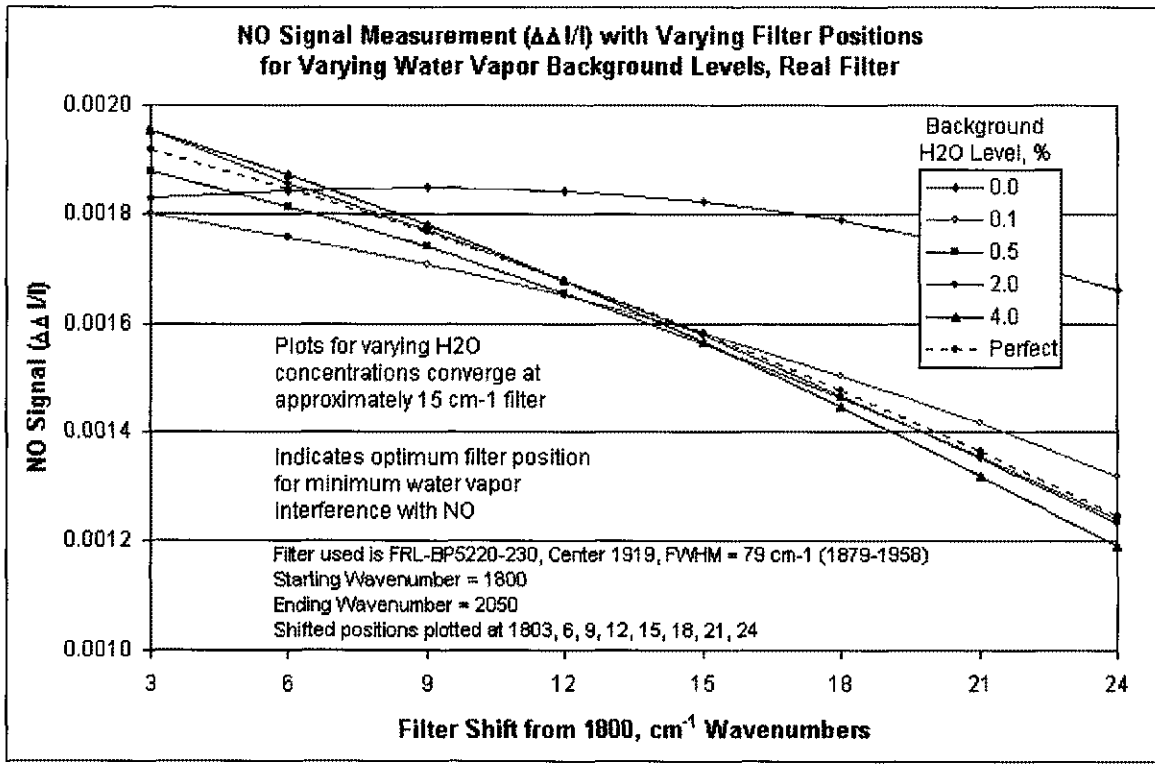

Figure III-9. H_2Ov Error Mitigation Filter Selection Plot

In Figure III-9, first note that the plots for each level of water vapor nearly converge around a 14- to15-wavenumber filter shift. In other words, with the filter in this position, different levels of background water vapor all have essentially the same effect on the measurement. In addition, at this point they converge with the dashed "perfect" line, which is a theoretical line representing the system response as if there were no water vapor at all in both the background and the plume. In other words, all the graphs converge to an ideal condition in which there is no effect from water vapor interference in the measurements. The closer a given plot is to the "perfect" plot, the more stable measurements are in the face of changing system parameters. For instance, the green plot for 2% water vapor tracks tightly to the "perfect" plot across the range of filter positions, so at this humidity level, filter specification could be very loose. Of course, our goal is immunity to changing water vapor levels, so it is important to maintain filter position in

the ~14 to 16 wavenumber shift region of convergence. Once adjusted, the major cause of filter shifting would be due to temperature fluctuation, but filter variations due temperature are expected to be within the design ±1 wavenumber range, based on discussions with potential filter suppliers.

The notable exception to the above analysis of Figure III-9 is the plot for zero background water vapor (dark blue), which diverges widely from the others. In this case, the exhaust plume adds the equivalent of about 300 ppm water vapor to a totally dry sample path, a large perturbation from the original path condition. A large water vapor error would thus result when making measurements under such conditions. In reality such extremely low humidity is rare except in very cold conditions. As shown by Table III-4, common temperature and humidity ranges are well within the predicted operational parameters. 50% relative humidity is a common level; so at 50° F and 50% RH, there is ½ (1.21%) = 0.6% background water vapor. In addition, the 0.1% H_2Ov plot on Figure III-9 is in the convergence zone, so very little background vapor is needed to ensure stable operation.

Table III-4. Vapor Pressure Change with Temperature

Temp °F	Temp °C	Saturated Vapor Pressure, Torr	H_2O% at 760 Torr Ambient
100	37.8	49.157	6.47%
90	32.2	36.068	4.75%
70	21.1	18.765	2.47%
50	10.0	9.209	1.21%
30	-1.1	4.227	0.56%
10	-12.2	1.804	0.24%

Note: Data from the 1988 edition of the CRC Handbook of Chemistry & Physics

Another, somewhat more intuitive view of the simulation data appears in Figure III-10, which plots constant filter position with respect to varying levels of background water vapor, and the resulting target NO measurements. The $\Delta\Delta I/I$ values shown earlier in Figure III-9 have been converted to parts-per-million NO. As indicated, the actual value of NO in the sample path is equivalent to 914.4 ppm; the values for measurements with the "optimized" filter position at 1815 cm^{-1} (dashed line) are seen to converge around the correct value. A goal of the project is to reduce H_2Ov artifact error to

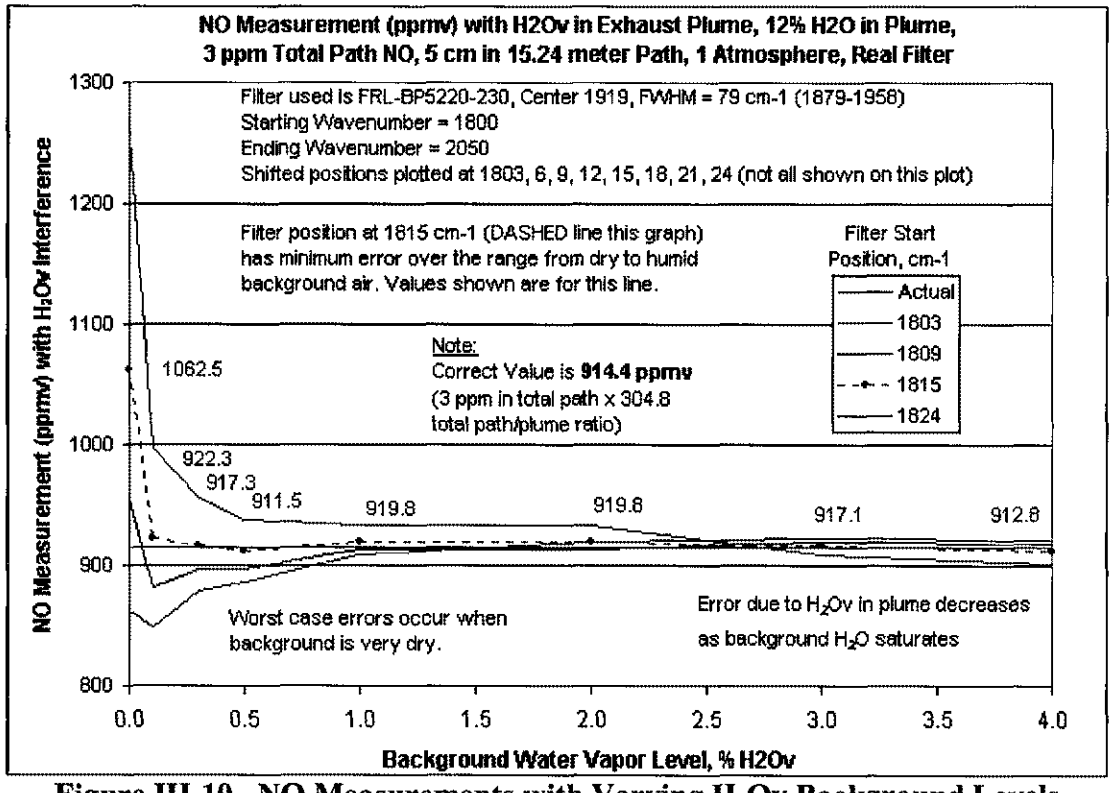

Figure III-10. NO Measurements with Varying H_2Ov Background Levels

±10ppm, achieved here down to 0.1% background water vapor, below which there is wide deviation from the true values. Error increases for different filter positions and with decreasing background water vapor. Higher background H_2Ov values across the path

place many of the H_2Ov lines in saturation; therefore, the exhaust vapor has less impact. In dry conditions the exhaust plume water vapor presents a greater perturbation of the total path and there is no benefit from water vapor absorption saturation, causing higher error values. A duplicate set of calculations was also run, but with atmospheric pressure set at 0.822 atmosphere to simulate high-altitude (1 mile elevation, e.g., Denver, Colorado) conditions. Results were essentially the same, and clearly indicated that a filter position of about 1814 is required for optimization.

The computer model predictions all consistently confirmed that it would be possible to "null out" the water vapor interference while remotely measuring nitric oxide in on-road automobile exhaust. The next stage of work was therefore to move forward with experimentally verifying the predictions that had been made with the computer model. These laboratory experimental results are described next in Chapter IV.

CHAPTER IV

LABORATORY EXPERIMENTS

The computer modeling and predictions discussed in Chapter III proceeded for several months prior to procuring all components and were used to determine the performance characteristics of parts that needed to be ordered. Once the system components had been received and fully characterized, we were able to better model the PMGFCR instrument and make more accurate predictions about its behavior. By that stage the laboratory instrument was operational and experimental comparisons with the model's predictions could be made. Due to the toxicity of nitric oxide it is impractical to make actual NO measurements within the laboratory. This work is directed toward demonstrating the optimized system's insensitivity to water vapor interference, rather than sensitivity to nitric oxide, which has previously been verified[10].

The predictions detailed in Chapter III indicated that the water vapor artifact signal while making NO measurements would be minimized in a balanced GFCR system with the 5220-230 bandpass filter shifted ~14 to 15 wavenumbers from its design specification. These calculations were based upon a 15.24-meter total path and a 5 cm gas plume. Our objective was to devise an experiment to duplicate the conditions and results of the predictions, but it was not feasible to control the background water vapor level of a path of this length in the laboratory. The true goal was to verify that the interference could be nullified, regardless of path length. We therefore designed an apparatus that would allow control of the conditions in a shorter 1.5-meter path and calculated a new set of predictions based on that distance. The major functional difference between the short and long paths is that there is much greater optical depth of

water vapor on the long path; a 1,000-ppm H_2Ov background across 15 meters will be about equivalent to 10,000 ppm on a 1.5-meter path. This actually was an advantage; it had been determined that filter selection was most critical in the "dry background" case. If the GFCR response could be made impervious to transient water vapor with low background humidity, it followed that the higher-humidity regime would present no difficulties.

4.1 Description of Experiment

The apparatus used for the experiment is diagramed in Figure IV-1. The four major subsystems are the infrared source on the right, the water vapor controlled path at the center, the GFCR instrument on the left, and the data acquisition system (DAS). The infrared source is a hot filament, essentially a black body radiating broadband infrared. The filament is placed at the focal point of a CaF_2 collimating optic that directs the collimated infrared beam down the vapor-controlled sample path. The path is valved to allow ambient (humid) air, dry air, or a mixture to flow through. Driven by a small inline fan, mixing and 0.8 second air changes are allowed. A compressed air tank supplies dry air, composed of standard air (~78% nitrogen, 20% oxygen, and 2% trace gases) verified to have minimal water vapor, measured to below the $-60^{o}C$ scale minimum on the dew point hygrometer, i.e., <25ppm H2Ov. A dry air holding tank contains a large volume of air between changes to ensure that both dry and room air flow through the path at the same velocity. The path is equipped with a hygrometer, flow meter, and thermometer to monitor the airflow through the system. From the path the beam enters the GFCR instrument where it is polarization modulated, split and directed through the correlation or vacuum cells, recombined, balanced, filtered, and focused onto the

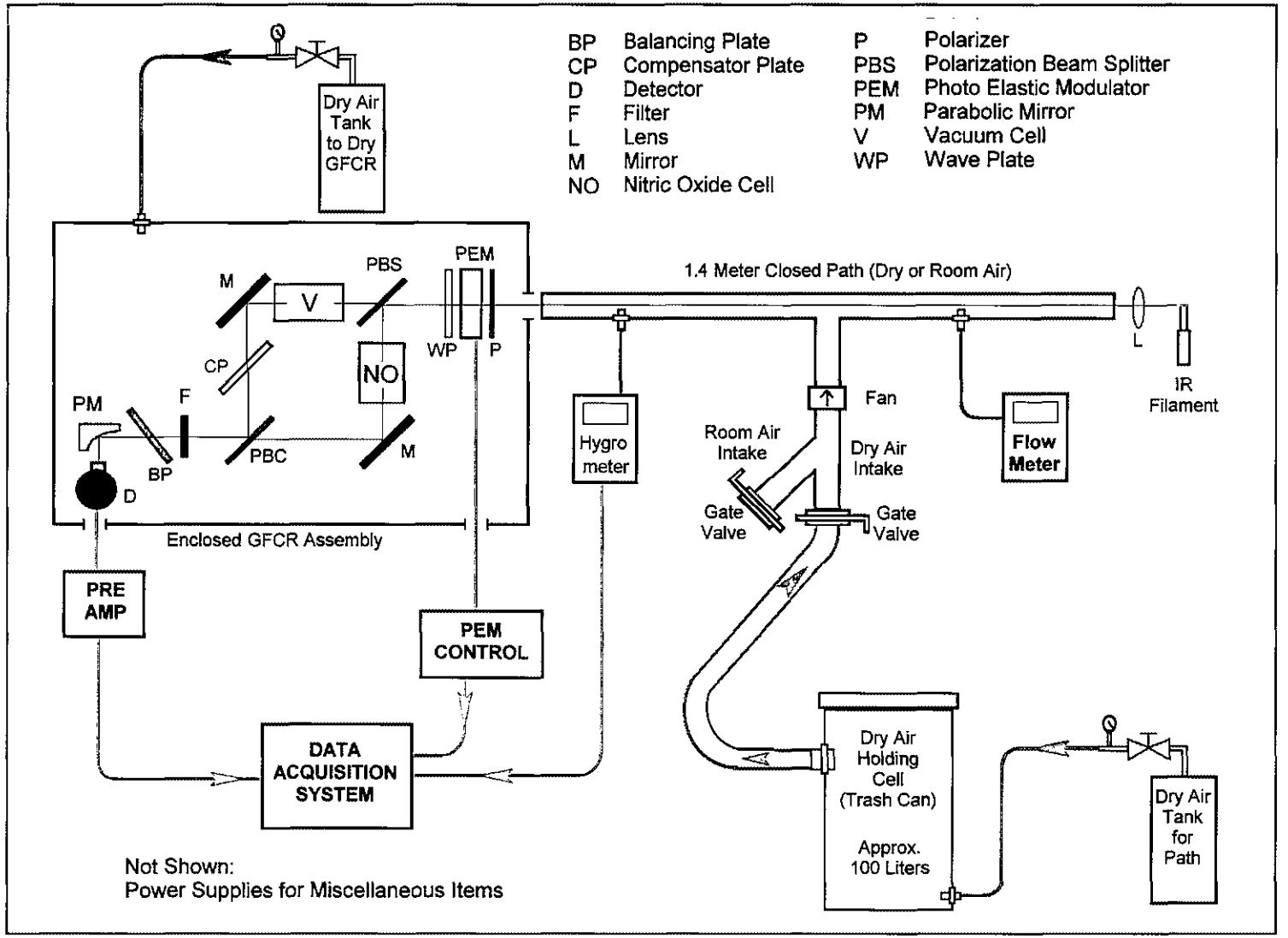

Figure IV-1. Short Path Controlled Water Vapor Experimental Setup.

photodetector. The detector output is phase-locked to the photoelastic modulator reference signal with a lock-in amplifier to get the ΔI signal (the AC voltage, or dV). The "I" total signal intensity is the detector DC voltage, or "V." Both values are captured with a data acquisition system (DAS) utilizing a National Instruments GPIB, and stored on the DAS computer for later analysis. Another channel of the DAS captures the output from the dew point hygrometer. During the testing process it became evident that the dew point hygrometer's response time was much too slow to be of any use on short time scales. As expected by the airflow rate, the GFCR ΔI response on the data acquisition display indicated path air changes were taking less than one second. The hygrometer's time to recover from a wet to a dry path measurement was in excess of twenty seconds; waiting for it to settle to a stable value significantly increased the time for each experiment. Though we would have preferred to have had a record of the path humidity on the DAS record file, we decided to rely on a hand-held hygrometer that exhibited faster response times. The humidity levels were manually recorded at each stage of the test.

After several tests series were performed, the apparatus described above was improved by replacing the open path forced air system with a closed cell that could be filled with dry or humid air, or evacuated. This was due to concern that operating the valves on the open path setup was jogging the PMGFCR assembly and affecting its alignment. This modification helped improve the consistency of the measurements.

The experimental process was to set the optical filter to a normal angle of incidence, balance the GFCR system to zero with the aid of the spectrum analyzer, and then alternately send dry air and ambient room air through the path. Initial tests were 60

seconds long, with the DAS set to sample at 100 Hz for 6000 data samples per test. Later tests were run for 10 seconds at 600 Hz to capture 6000 samples. This sequence was then repeated with the filter tilted 2.5° more in each successive test, for a total 20 degree tilt range, also corresponding (non-linearly) to about a 20 wavenumber filter shift.

4.2 Experimental Results

For each test, the DAS collected 6000 samples (an arbitrarily chosen number) of the dV and V signals from the PMGFCR instrument. This data was imported into a spreadsheet to determine the dV/V ratio for each measurement. The true dV/V value is

$$\frac{dV}{V} = \frac{dV_{path}}{V_{path} - V_{blocked}}, \tag{4.1}$$

where dV_{path} and V_{path} are the measurements taken through the sampling path, while $V_{blocked}$ is the detector DC voltage output with the infrared source blocked. $V_{blocked}$ is due to background light in the path, and to detector noise (the potential measurement effects of these noise sources will be discussed later). The background voltage must be subtracted so that the V value used in the calculations is due only to light from the beam passing through the target path.

Cooling with 77°K liquid nitrogen minimizes the detector noise, but all noise sources cannot be eliminated. The overall measured blocked-beam noise is Gaussian with a mean value of zero, and thus is eliminated from the final measurements by averaging. However, with measured noise deviations σ on the order ~5 μV with a 1kHz filter on the detector output, it does have an effect the precision of the measurements. Assuming a 2σ noise of 10 μV, a typical ($V_{path} - V_{blocked}$) of 1.5 volts, PMGFCR response

function slope of 0.00055/ppm, and a path/plume ratio of 300, the NO ppm-equivalent signal due to background stray light and thermal noise would be

$$[(10\text{x}10^{6} \text{ volts} / 1.5 \text{ volts}) / 0.00055 \text{ ppm}^{-1}] \text{ x } 300 = 3.64 \text{ ppm NO error.}$$

Since the instrument's goal is an overall sensitivity of ±10 ppm NO, the need to minimize systematic errors such as that of the water vapor interference is evident.

The calculated average dV/V for the "wet" test is subtracted from that of the "dry" (no interference) test to get the differential signal due to the interference. These values are plotted versus the filter tilt or filter wavenumber shift. Figure IV-2 shows the experimental data from one test series.

The system was balanced at each filter setting with a "wet" path. The blue plot for the "wet" dV/V measurements is nearly zero for all measurements, indicating that the balancing plate was performing as designed. The solid red dry-wet plot (ΔΔV/V) slopes down, crossing through zero at approximately a 6-wavenumber shift. At first glance,

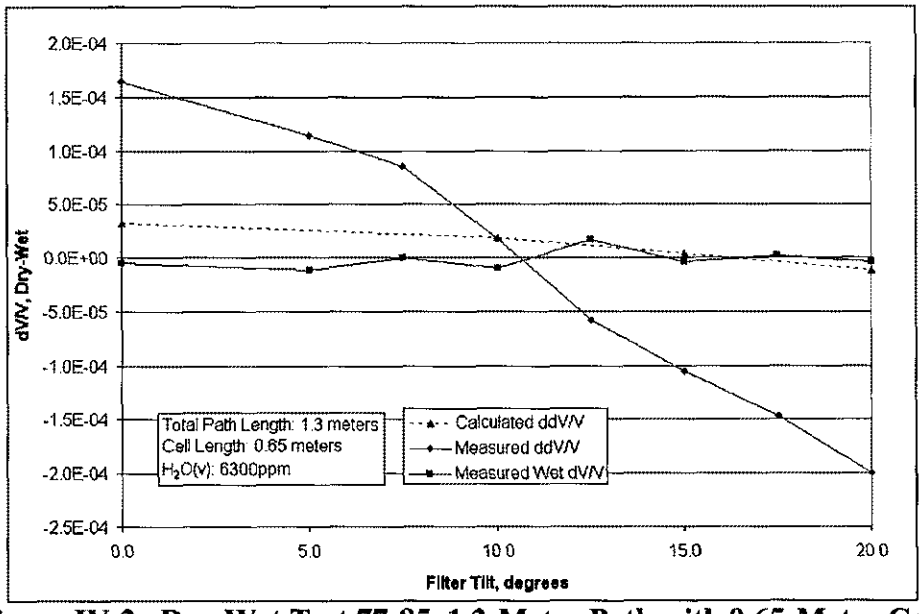

Figure IV-2. Dry-Wet Test 77-85, 1.3-Meter Path with 0.65-Meter Cell.

therefore, Figure IV-2 appears to show that our goal of balancing to zero and eliminating water vapor artifact signals had been achieved. However, the computer simulation data for this test differed significantly from the experimental results. The experimental $\Delta\Delta V/V$ values were approximately 4.5 times greater magnitude than the model's predictions, shown dashed in Figure IV-2. Several experimental test series consistently gave such "scaled-up" results. In addition, tests with higher background water vapor concentrations did not exhibit as much "leveling" due to water vapor saturation as had been expected.

To attempt to explain the disparity between the experiment and the computer model, we first re-did the simulations and achieved the same results as before. Next, the calculations were performed directly on HITRAN-PC and MSExcel without the PMGFCR model, with results again consistent with previous calculations. We also had a high degree of confidence in the computer model due to its previous success in modeling the measurements of a CO_2-sensing PMGFCR. We therefore looked to the experimental apparatus for a means to explain the difference between the measured and modeled data.

4.3 Investigation of Systematic Errors

The three elements of the instrument most likely to cause the measurement disparity are the detector, the correlation cell, and the optical filter. If the wrong detector were being used, the measurements made would not have been looking at the correct spectral region and thus would not conform to our predictions. However, the detector could be readily ruled out since the serial number indicated it was the 5.2 μm detector we believed it to be, and thorough manufacturer's documentation was on file.

Next, if the correlation cell installed in the PMGFCR were not actually filled with NO, the differential absorption signal between the two polarized paths would behave differently than expected. We verified that the cell was in fact the NO cell that had been characterized previously in the FTIR spectrometer. During the period of this investigation we received two more correlation cells from the contractor who had been working on improving upon the combination NO-NO_2 cells. Both new cells were scanned in the spectrometer to verify they contained NO, and then used in a test series in the PMGFCR, with results consistent with those found earlier using the original cell.

By this point the optical filter was the prime suspect for a systematic error source. If the wrong filter were to be used, the measurements would not be targeting NO absorption features and thus would differ from the predicted results. Several different filters used in the GFCR Lab look identical but have different optical pass bands. Again the spectrometer was utilized, verifying that the correct 5220-230 filter had been used. Further investigations were called for.

Since the filter was tilt tuned in order to shift its bandpass to higher wavenumbers, we began to investigate other effects of tilting the filter, particularly effects associated with the orientation of the incident light's polarization with respect to the filter (i.e., either p- or s-wave orientation). The filter was placed in line with a linear polarizer in the FTIR spectrometer's collimator and scanned at incremented angles of incidence, as was performed previously with unpolarized light (as shown in Figure III-4). The filter behavior was found to have a strong dependence on the polarization orientation of incident light with respect to the tilted filter, as seen in Figures IV-3A and B.

Inspection of Figure IV-3A reveals that the filter exhibits markedly different

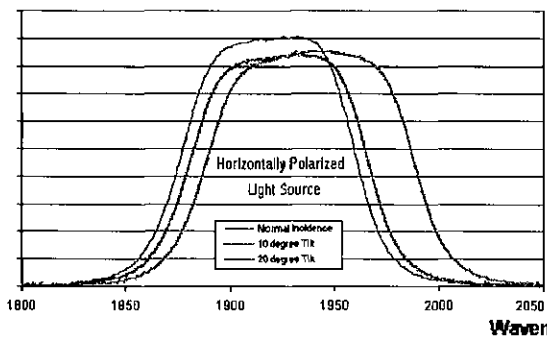

Fig. IV-3A. Optical Filter Shift with Tilt and Horizontally Polarized Light.

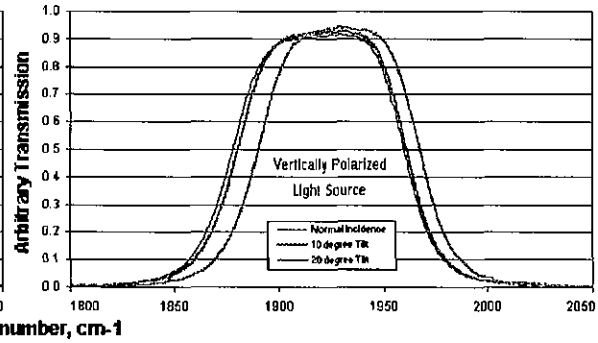

Fig. IV-3B. Optical Filter Shift with Tilt and Vertically Polarized Light.

performance transmitting vertically polarized light (s orientation in this case) and horizontally polarized light (p orientation). At normal incidence, the filter bandpass is the same for both polarizations. With p-orientation, as the filter is tilted, the bandpass broadens and transmission decreases. However, with s-orientation it slightly narrows and transmission slightly increases. Both polarization orientations manifest an increasing shift in wavenumber with tilt, though to varying degrees.

It was evident that a great deal of the larger-than-expected $\Delta\Delta V/V$ measurement was the result of the sensitivity of the filter to the incident polarization orientation. Since the PEM is switching the light polarization between vertical and horizontal, as the filter is tilted it creates a situation where the incident light on the filter alternately switches from p- to s-orientation. This switching effectively causes the detector to alternately switch between two slightly different filter bandpasses when making the differential path measurements. This is contrary to the basic concept of gas filter correlation measurements, to view the *same* spectral region through two different gas cells so that the differential signal measured is attributable only to the target gas in the sampling path.

To verify that the variable filter shift was responsible for the high measurements,

new computer simulations were performed with each light polarization passing through its respective bandpass. These revised calculations were then compared to the experimental data already gathered and processed. Figure IV-4 presents the same ΔΔV/V experimental data shown earlier on Figure IV-2, but plotted with respect to filter tilt

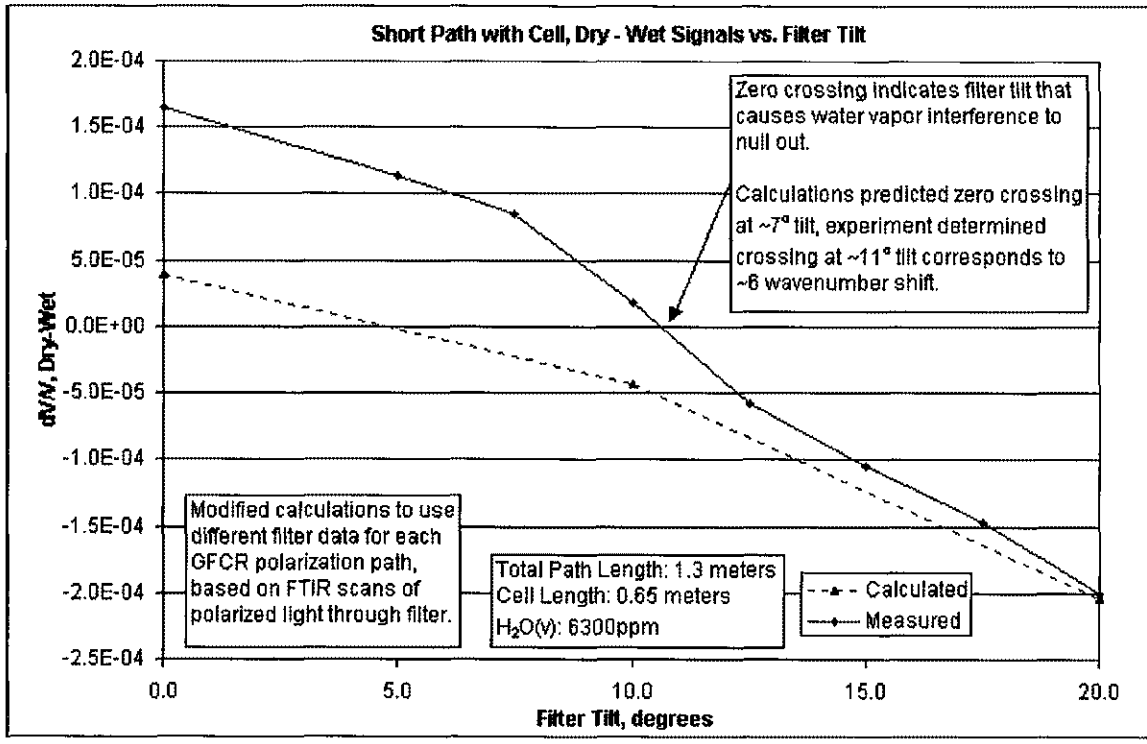

Figure IV-4. Short Path ΔΔV/V Experimental and Revised Calculated Data

rather than wavenumber shift. This was done to simplify the modeling with the polarization-sensitive filter, since tilt was a controllable parameter but filter wavenumber shifting varied with polarization. Although the magnitude of the small tilt-angle data is off by about a factor of 3, the slope of the experimental and modeled data are more similar. The zero-crossing for both plots agrees better than in the earlier model, and the plots at higher tilt angles nearly coincide. Overall, there is a better than 50% improvement in agreement versus the earlier model without the polarization effects.

CHAPTER V

CONCLUSIONS

The major obstacles in previous attempts by others to measure NO in the infrared region for vehicular exhaust analysis were slow GFCR channel switching and interference from spectral overlap of NO by H_2Ov. The PMGFCR technique for measuring NO had been demonstrated in a controlled laboratory setting at the NASA Langley GFCR Lab, showing that this method had the inherent specificity and high switching rate to have the potential to allow on-road measurement of NO. This thesis has addressed a theoretical means of optimizing the PMGFCR to mitigate the interfering effects of H_2Ov.

The two main goals set for this research have both been achieved, to varying degrees. Objective #1 was to verify that it is possible to null out $H_2O(v)$ interference by making use of the positive and negative effect of the interference on PMGFCR measurements. Three steps were taken to accomplish this goal. The preliminary model helped give insight into how the interfering lines interact with the correlation cell absorption spectrum, and how cell fill pressures influence this interaction. Next, extensive simulations with the NASA LaRC GFCR Response Model applied a wide range of background water vapor levels, gas cell pressures, and filter positions to the system to evaluate how they interact to effect a stable insensitivity to H_2Ov. Based on the predictions made with the model, an laboratory bench top experiment was designed to test these affects. The experiments were successful in mitigating water vapor interference, but also revealed areas that require careful consideration while making use of the PMGFCR technique, particularly polarization sensitivity of the optical

components. More work is planned to address these concerns fully, but the basic goal was achieved.

The second major objective was to evaluate the accuracy of the predictions made with the computer-modeled spectroscopy calculations. The GFCR response model proved invaluable in conducting this research, both in ease of use and in helping determine and confirm the sources of systematic errors in the experimental process. Its continued use and development is an asset to this research.

The PMGFCR technique still needs some details ironed out before it will be ready for making precise on-road measurements of NO in vehicular exhaust. The next step is to find a means of avoiding the polarization sensitivity exhibited by the optical filter. Work toward achieving this objective is currently underway, and involves orienting the tilt of the filter to ensure equal amounts of s- and p-wave light are incident on the filter, minimizing the bandpass distortions caused by its polarization sensitivity.

In addition, design work continues on the NASA/SPX on-road multi-channel PMGFCR instrument, of which the NO system investigated here is just one part.

LIST OF REFERENCES

1. Stern, A.C. ed., *Air Pollution, Second Edition*, Academic Press, NY, 1968.
2. Peterson, M. A. et al, *Effects of Air Pollution and Acid Rain on Fish, Wildlife, and Their Habitats,* United States Environmental Protection Agency, 1982.
3. Hansen, J., et al, "Climate Impacts of Increasing Carbon Dioxide," *Science*, 1981, **213**, 957-966.
4. Pokharel, S.S., Bishop, G.A., and Stedman, D.H., On-Road Remote Sensing of Automobile Emissions in the Denver Area: Year 2 (draft), Coordinating Research Council, 2000.
5. United States Environmental Protection Agency. *National Air Pollution Emission Trends, 1900-1996*, 1997, EPA-454/R-97-011.
6. Bishop, G.A., Pokharel, S.S., and Stedman, D.H., On-Road Remote Sensing of Automobile Emissions in the Los Angeles Area: Year 1 *(draft)*, Coordinating Research Council Project E-23-4, 2000.
7. Popp, P.J., Bishop, G.A., and Stedman, D.H., *Proceedings of the 7th CRC On-Road Vehicle Emissions Workshop*, 1997, **7**, 4-1.
8. Russell, J.M., et al, *Journal of Geophysical Research*, 1993, **98**, D6, 10.777.
9. Sachse, G.W., and Wang, L., *Proceedings of OSA Conference on Optical Remote Sensing of the Atmosphere*, 1990.
10. Sachse, G.W., LeBel, P., Steele, T., Rana, M., *Proceedings of the 8th CRC On-Road Vehicle Emissions Workshop*, 1998, **8**.
11. Verdeyen, J.T., "Laser Electronics," Prentice Hall, New Jersey, 1995.
12. Bullock, A.M., *"High Resolution Wavelength Modulation Spectroscopy for Precise Gaseous Characterization,"* ODU Master's Thesis, 1997.
13. Svanberg, S., "Atomic and Molecular Spectroscopy: Basic Aspects and Practical Applications," Berlin, 1992.
14. Saleh, B.A., and Teich, M.C., "Fundamentals of Photonics," John Wiley & Sons, Inc. New York, 1991.

15. Sachse, G.W., NASA LaRC GFCR Laboratory, personal conversations, 2000.

16. Information from the Hinds, Inc. Model PEM-90 Photoelastic Modulator User's Manual, 1999.

17. Rothman, L.S., et al, "The HITRAN Molecular Spectroscopic Database and HAWKS," *JQSRT*, 1998, **60**, 665-710.

18. Ontar Corporation website, http://www.ontar.com, 2000.

19. Spectrogon, Inc. website, http://www.spectrogon.com/opfilter.html, 2001.

20. Braker, W., and Mossman, A.L., "Matheson Gas Data Book," Matheson Gas Products, New Jersey, 1971.

21. Shen, L.C., and Kong, J.A., "Applied Electromagnetism, Third Edition," PWS Publishing Company, Boston, Massachusetts, 1995.

CURRICULUM VITA
for
DAVID K. LOCKWOOD

DEGREES:

Master of Science (Electrical Engineering), Old Dominion University, Norfolk, Virginia, May 2001.
Bachelor of Science (Electrical Engineering), Old Dominion University, Norfolk, Virginia, May 2000.
Bachelor of Arts (Art History), Virginia Polytechnic Institute and State University, Blacksburg, Virginia, December 1989.

PROFESSIONAL CHRONOLOGY:

Project Manager, Infinity Design Group, Newport News, Virginia, 1998-2001.
Electrical Designer, Apex Engineering, Newport News, Virginia, 1996-1998.
Electrical Designer, ECI Engineers, Newport News, Virginia, 1989-1996.

SCIENTIFIC AND PROFESSIONAL SOCIETIES MEMBERSHIP:

Member, Eta Kappa Nu Electrical Engineering Honor Society.
Member, Virginia Society of Professional Engineers (VSPE).
Member, American Institute of Aeronautics and Astronautics (AIAA).
Member, Institute of Electrical and Electronics Engineers (IEEE).

HONORS AND AWARDS:

Old Dominion University Kovner Award for Electrical Engineering, 2000.
Hampton Roads IEEE Student Paper Contest, Second Place, 2000.
ODU ECE Department Senior Design Team Project, First Place, 1999.
Old Dominion University Stuart Russell Scholarship for Electrical Engineering, 1999.

MAJOR SERVICE ACTIVITIES:

Old Dominion University Engineering Ambassadors, 2001.
National Marrow Donor Program, 2000.
American Cancer Society Walk for Life, 1998-2000.
Our Lady of Mount Carmel Church Hospitality Committee, 1996-Present.
Virginia Tech Campus Art Advisory Board, 1988-1989.

GRANTS AND CONTRACTS AWARDED:

NASA Graduate Student Researchers Program, 2000.
Virginia Space Grant Consortium Project Support Award, 1999.
United States Air Force ROTC Scholarship, 1984.

SCHOLARLY ACTIVITIES COMPLETED:

11^{th} Coordinating Research Council On-Road Vehicle Emissions Workshop, poster session presented with G.W. Sachse, San Diego, California, 2001.